Title page

Targeting ARF4-mediated intracellular transport as a broad-spectrum antiviral strategy

Ming-Yuan Li[1,2#], Kao Deng[1#], Xiao-He Cheng[1#], Lewis Yu-Lam Siu[3], Zhuo-Ran Gao[2], Trupti Shivaprasad Naik[3], Viktoriya G Stancheva[4], Peter Pak-Hang Cheung[2], Qi-Wen Teo[3], Sophie Wilhelmina van Leur[4], Ho-Him Wong[3], Yun Lan[3,5], Tommy Tsan-Yuk Lam[3,5] Meng-Xu Sun[1], Na-Na Zhang[1], Yue Zhang[1], Tian-Shu Cao[1], Fan Yang[6], Yong-Qiang Deng[1], Sumana Sanyal [4*] and Cheng-Feng Qin [1,7*]

Affiliations

1 State Key Laboratory of Pathogen and Biosecurity, Beijing Institute of Microbiology and Epidemiology, Beijing 100071, China.

2 Department of Chemical Pathology and Li Ka Shing Institute of Health Sciences, Chinese University of Hong Kong, Hong Kong SAR, China

3 HKU-Pasteur Research Pole, School of Public Health, Li Ka Shing Faculty of Medicine, The University of Hong Kong, Hong Kong SAR, China.

4 Sir William Dunn School of Pathology, University of Oxford, South Parks Road, Oxford OX1 3RE, UK.

5 Centre for Immunology & Infection, Hong Kong Science and Technology Park, Hong Kong SAR, China

6 Institute of Pathogenic Biology, Shenzhen Center for Disease Prevention and Control, Shenzhen, China

7 Research Unit of Discovery and Tracing of Natural Focus Diseases, Chinese Academy of Medical Sciences, Beijing 100071, China

[#]These authors contributed equally to this work and shared the first authorship.

*Corresponding author: Cheng-Feng Qin (qincf@bmi.ac.cn) and Sumana Sanyal (sumana.sanyal@path.ox.ac.uk)

Summary

Host factors that regulate cellular vesicular trafficking contribute to progeny virions' destination, thus representing potential antiviral drug targets. Here we demonstrate that genetic deletion of ARF4, a regulator of vesicle transport, suppresses infections by multiple pathogenic RNA viruses including Zika virus (ZIKV), influenza A virus (IAV), Vesicular Stomatitis virus (VSV) and severe acute respiratory syndrome coronavirus 2 (SARS-CoV-2). Viral infection stimulates ARF4 activation, and viral production is rescued when cells are reconstituted with activate ARF4, but not with inactivate mutants. Mechanistically, ARF4 deletion disrupts viral translocation to the Golgi complex, and leads to mis-sorting for lysosomal degradation, thereby blocking virus release. Importantly, peptides targeting ARF4 demonstrate substantial therapeutic efficacy in mice against ZIKV and IAV challenge by inhibiting ARF4 activation. Our findings highlight the crucial role of ARF4 in viral infection, presenting it as a potential broad-spectrum antiviral target for further pharmaceutical development.

Introduction

Due to the lack of effective vaccines or antiviral medications, pathogenic RNA viruses like flaviviruses, coronaviruses, and influenza viruses often cause epidemics and pandemics [1-5]. RNA viruses exhibit a higher mutation rate compared to DNA viruses, resulting in accelerated evolution and the development of drug resistance. Thus, traditional antiviral approaches that target viral proteases/polymerases to inhibit the function of viral proteins encounter difficulties[6,7]. Antiviral medications that target host dependency factors are therefore compelling substitute tactics. Viruses frequently exhibit overlap when it comes to manipulating host cellular functions. Thus, inhibitors that specifically target crucial host factors, such as human Dihydroorotate dehydrogenase (DHODH), have the ability to effectively combat a wide range of pathogenic viruses[8,9]. One major drawback of this approach is the potential risk of drug toxicity or adverse side effects on the host, as selected host factors are typically essential for their own biological processes[10-13]. Achieving specificity and reducing unintended impacts is a major obstacle. Therefore, ideal host targets should be sequestered in normal cellular processes or be replaceable with their homologous analogues. Lastly, limited knowledge on the mechanisms underlying viral manipulation of host cell biology and the biochemical underpinnings of host-pathogen interactions has continued to impede the development of novel antiviral approaches.

The ADP-ribosylation factors (ARFs), which are small GTPases that belong to the Ras superfamily, are known to control intracellular vesicular transport and organelle structure [14]. ARFs are activated upon GTP binding, which enables them to be recruited to intracellular membranes, such as the plasma membrane and other organelles [15]. Based on the identity of their amino acid sequences, mammalian ARFs are classified into three classes: Class I ARF proteins (ARF1-3), Class II (ARF4-5), and Class III (ARF6)[14]. Previously, mouse hepatitis coronavirus and coxsackievirus were shown to hijack and manipulate the ARF1 associated signalling pathway [16,17]. Due to high sequence conservation, ARF4 and ARF5 have confounded efforts to define their individual roles. By enlisting coat components and packaging cargo for transport to post-Golgi compartments, they are expected to aid in early Golgi transport [14]. Our previous study has shown that Class II ARFs are involved in the

secretion of Dengue virus (DENV), a member of flaviviruses [18,19]. However, the exact role of Class II ARFs during RNA virus infection remains to be investigated.

In this study, we show that ARF4, but not ARF5, is essential for the infection and pathogenesis of multiple pathogenic RNA viruses, including ZIKV, IAV, SARS-CoV-2 and VSV. Mechanistic studies revealed that the activation of ARF4 guided precise sorting and intracellular transport of progeny virions. Most importantly, ARF4-targeting peptides designed to block its activation showed a pan antiviral effect in both *in vitro* and *in vivo* systems. Thus, the pivotal function of ARF4 exposes a critical vulnerability in the infection of RNA viruses, which provides the foundation for broad-spectrum antivirals against human diseases.

Results

ARF4, not ARF5, is required for *in vitro* and *in vivo* ZIKV infection

To clarify the role of class II ADP-ribosylation factors (ARF4 and ARF5) in ZIKV infection, we generated CRISPR-Cas9 mediated knock-outs of ARF4 and ARF5 in Vero cells respectively **(Extended Data Fig.1),** and then challenged them with ZIKV. ARF4, but not ARF5 deletion was found to protect cells from ZIKV induced cytopathic effect (CPE), implying a vital role of ARF4 in ZIKV infection **(Fig. 1a).** Compared to wild-type (WT) cells, production of infectious ZIKV progeny virions titrated by plaque assay was dramatically reduced (~2-4 logs) and stalled in ARF4 knock-out ($ARF4^{-/-}$), but not in ARF5 knock-out ($ARF5^{-/-}$) cells **(Fig. 1b-c).** In addition, ARF4 deletion in HeLa cells also resulted in a notable reduction of ZIKV infection **(Extended Data Fig.2).**

To further investigate the importance of ARF4 *in vivo*, we utilized the Cre-loxP system to generate tissue-specific knock-out ARF4-flox/cre-Prok2 (fl+Prok2) mice. Transcription of ARF4, but not ARF5 was largely reduced in the two main ZIKV-targeting tissues-brain and testis **(Extended Data Fig.3).** Mice were pre-treated with an anti-mouse IFNAR1 antibody a day before ZIKV challenge, which suppressed type I IFN responses, facilitating successful ZIKV infection and associated pathogenesis **(Fig. 1d)**[20]. This ZIKV infection mouse model was

then used for subsequent animal infection experiments. Compared to ARF4-flox (fl) control mice, ZIKV induced viremia measured in serum samples at 2, 4, and 6 days p.i. was significantly restrained in fl+Prok2 mice **(Fig. 1e).** As expected, viral load in brain and testis of fl+Prok2 mice was substantially reduced, particularly at day 6 post infection **(Fig. 1f).** Importantly, inflammatory cell infiltration in brain, typically associated with ZIKV induced pathogenesis, was absent in fl+Prok2 mice **(Fig. 1g left panel).** Moreover, necrotic seminiferous tubules, another ZIKV induced pathological abnormality, were observed in testis of ZIKV infected control mice, but not in fl+Prok2 mice **(Fig. 1g right panel)**. Collectively, these data demonstrate that ARF4 is a vital host factor that facilitate its infection *in vitro* and *in vivo*.

ZIKV activates ARF4 to facilitate its infection

Subsequent investigations were aimed to determine the underpinnings of ARF4 function in ZIKV infection. Our previous studies showed that ARF4 binds to a structural protein of another member of flavivirus, DENV, to initiate the ER-to-Golgi transport of progeny virions[19]. Therefore, we firstly checked the interaction(s) between ARF4 and ZIKV proteins by performing immunoprecipitation to pull down endogenous ARF4 using its specific antibody. However, none of viral structure proteins was co-immunoprecipitated, suggesting the role of ARF4 in ZIKV infection differs from that in DENV **(Extended Data Fig.4).** We then co-stained the ZIKV structural E protein and endogenous ARF4 to check their intracellular translocation during viral infection. Compared to mock-infected cells where endogenous ARF4 is uniformly distributed in the cytoplasm, ZIKV infection triggered a re-distribution of ARF4 that correlated with ZIKV E proteins (**Extended Data Fig.5**). This data suggests that host ARF4 is manipulated by ZIKV, potentially resulting in alterations to its biological status and functions.

ARF4 is known to switch between its active GTP-bound form and inactive GDP-bound form. To ascertain the status of ARF4 during ZIKV infection, activated ARF4 were pulled down and measured by using GST fused with VHS-GAT domain of GGA3 **(Fig. 2a)**, a Golgi-associated coat protein that has been shown to bind to GTP-bound ARFs[15,21,22]. As shown in **Fig. 2b-c,** ZIKV infection led to significant increase in activated ARF4 compared with the mock group. To test whether ZIKV infection relies on the activation of ARF4, we reconstituted and stably expressed wide type ARF4, as well as two mutants-T31N and Q71I

into the ARF4$^{-/-}$ cells which maintained ARF4 in inactivated and activated states respectively **(Fig. 2d)**[15]. All reconstituted ARF4 WT and mutants were expressed at similar levels in ARF4$^{-/-}$ cells **(Extended Data Fig.6a)**. ZIKV infection was performed in these genetically modified cells together with their parental ARF4$^{-/-}$ and Vero cells as a negative and positive controls, respectively. Plaque assay results showed that, compared to the viral titer measured in WT and ARF4$^{-/-}$ samples, production of progeny virus was efficiently rescued in ARF4 WT and Q71I expressing cells, but not in T31N expressing cells **(Fig. 2e),** indicating that ZIKV infection relies on the activation of ARF4. To confirm this, ARF4 WT and T31N were stably overexpressed in Vero cells and then challenged by ZIKV **(Fig. 2f and Extended Data Fig.6b).** As expected, the number of progeny virions was slightly escalated in ARF4 WT overexpressing cells, but significantly restrained in T31N overexpressing cells **(Fig. 2g).** Collectively, these data demonstrate that ZIKV infection leads to the re-distribution and activation of endogenous ARF4, which in turn, facilitates its subsequent life cycle.

ARF4 orchestrates the intracellular transport and secretion of progeny virions.

To delve deeper into the role of ARF4 in ZIKV infectious life cycle, we firstly quantified the intracellular viruses in ARF4-deleted cells by RT-qPCR using ZIKV specific primers. Contrary to the significant decrease of progeny virions in culture medium (**Fig.1b**), ARF4 absence or inactivation did not change the quantity of viral RNA copies in infected cells **(Extended Data Fig.7).** Further validation with ZIKV replicon [23] in WT and ARF4$^{-/-}$ Vero cells showed that ARF4 has no direct impact on viral replication **(Extended Data Fig.8).** As ARF4 and ARF5 have been linked to the secretion of DENV[19], we hereafter investigated the specific role of ARF4 in regulating the egress of ZIKV. We stably expressed ZIKV prM and E proteins and isolated single clones in Vero WT and ARF4$^{-/-}$ cells, respectively (**Fig. 3a**). Stably expressed ZIKV prM and E have been confirmed to form non-infectious recombinant subviral particles (RSPs) which traffic along the same compartments as infectious ZIKV[18,24]. Although similar levels of ZIKV E proteins detected in cell lysate (CL) from both WT and ARF4$^{-/-}$ cells , secreted E detected in SN was rarely detected from ARF4$^{-/-}$ cells and RSPs secretion calculated as the percentage of E in SN in total E (SN+CL) was almost completely blocked in the absence of ARF4 **(Fig. 3b-c)**. To exclude the possibility that ARF4 deletion interfered with intracellular protein secretion through the constitutive pathway, we assessed secretion of ZIKV NS1 protein, as well as a non-viral protein: signal peptide fused horseradish peroxidase

(ssHRP) whose release occurs along the constitutive secretory pathway[19,25]. VHS-GAT fused GST pull-down showed that neither NS1 nor ssHRP expression stimulated the activation of ARF4 **(Extended Data Fig.9 a-d).** Importantly, no difference in either NS1 or ssHRP secretion were detected in ARF4-deficient cells **(Extended Data Fig.9 e-g).** These results indicate that while ARF4 is not necessary for bulk protein secretion *via* the constitutive pathway, it specifically regulates secretion of ZIKV progeny virions.

Transmission electron microscopy (TEM) was employed to visualize intracellular progeny virions. In both WT and ARF4$^{-/-}$ cells, virions measuring approximately 50 nm electron-dense dots were observed either in the ER lumen, or packaged into a vesicle generated by ER invaginations (**Fig. 3d and Extended Data Fig.10a**). To further expand these findings, a freeze-and-thaw (F&T) assay was conducted as previously described[25] using ZIKV infected or RSP- producing cells. Sub-organelle membranes were disrupted during F&T cycles which leads to the release of viral particles into the cytosol fraction, while unpacked viral structural proteins remain in separated membrane fractions[25] (**Fig.3e**). Our results indicated that the quantities of both viral RNA and infectious virions in cytosol fraction were comparable between WT and ARF4$^{-/-}$ cells, verifying that the depletion of ARF4 does not impact viral assembly. **(Fig. 3f and Extended Data Fig.10b**) Moreover, an increase of E protein was found in assembled RSPs from ARF4$^{-/-}$ cells suggesting ARF4 deficiency might impede intracellular transport and release of viral particles **(Fig. 3g and Extended Data Fig.10c).**

Considering the rate-limiting step in intracellular transport of progeny ZIKV is ER-to Golgi transport and trafficking across Golgi complex, we co-stained the viral E protein together with either trans-Golgi network marker-TGN46 or cis-Golgi marker-GM130 in ZIKV infected and RSP-producing cells respectively. E-stained condensed structures were observed, partially co-localizing with TGN46 or GM130 -stained Golgi complex, indicating arrival of newly assembled viral particles into the Golgi complex (**Fig. 3h and j upper panel**). In contrast, the E-staining were fragmented and rarely localized to the Golgi in the ARF4$^{-/-}$ cells (**Fig. 3h and j lower panel**). Significantly, the percentage of E protein co-localized with Golgi apparatus was reduced by more than 50% in ARF4$^{-/-}$ cells compared to WT cells (**Fig. 3i and K**). Concurrently, a decrease in prM cleavage leading to the formation of M protein, indicative of viral maturation in trans-Golgi network, was observed in ARF4$^{-/-}$ cells **(Extended Data Fig.11)**. Collectively, these data indicates that ARF4 harmonizes the sorting of newly

192 formed viral particles into the "correct" intracellular trafficking routes to achieve successful
193 viral maturation and egress.

194 **ARF4 deficiency leads to mis-sorting of progeny virions.**

195 Interestingly, TEM observations revealed that in ZIKV infected WT Vero cells, virion
196 embedded vesicles accumulated as a cluster into early endosome (EE) like vesicles **(Fig. 4a**
197 **and Extended Data Fig.12 upper panel).** However, in ARF4$^{-/-}$ Vero cells, similar clusters and
198 free virions were more frequently in late endosome/multivesicular bodies (LE/MVBs)-like
199 vesicles surrounded by lysosomes, indicative of degradation. **(Fig. 4a and Extended Data**
200 **Fig.12 lower panel).** In WT cells, clusters of virion-embedded vesicles were also visualized
201 being release from the cell surface **(Fig. 4b and Extended Data Fig.13 upper panel).**
202 Although similar membrane protrusions were observed in both ZIKV infected ARF4$^{-/-}$ and
203 uninfected WT/ARF4$^{-/-}$ cells, they were devoid of any virions **(Figure 4b and Extended Data**
204 **Fig.13 lower panel).** Moreover, transcriptome analysis by performing RNA-Seq using ZIKV
205 infected WT or ARF4$^{-/-}$ cells also indicated that genes related to lysosomal degradation were
206 enriched by GO analysis **(Fig. 4c)** and up-regulated in ARF4 $^{-/-}$ cells **(Extended Data Fig.14).**
207 Therefore, we speculated that ARF4-deficiency results in mis-sorting of virions into LE/MVBs,
208 for subsequent degradation in lysosomes. To verify this hypothesis, lysosomal degradation
209 was inhibited in ARF4$^{-/-}$ cells by using lysosome inhibitor-chloroquine. Results showed that,
210 compared to ZIKV infected WT cells, viral egress was rescued in ARF4$^{-/-}$ cells upon
211 chloroquine treatment to block lysosomal degradation, but not with MG132 to block
212 proteasome degradation **(Fig. 4d-e and Extended Data Fig.15).** We then analysed the
213 alterations in subcellular distribution of newly formed viral particles in ARF4$^{-/-}$ cells by
214 conducting biochemical fractionations through serial density gradient centrifugation, as
215 previously described [24]. This strategy allowed effective separation of membranes of the
216 secretory and lysosomal compartments from ZIKV infected cells, verifyied by their specific
217 markers. Results indicated that the viral E protein primarily co-migrated with the ER marker
218 in WT cells, whereas ARF4 deficiency caused a noticeable shift in the migration of E from ER
219 to lysosomal fractions, as verified by the anti-LAMP2 antibody. **(Fig.4f).** Finally, we
220 performed immunofluorescence imaging by co-staining the ZIKV E protein with EEA1 or
221 LAMP2, which are markers of early endosome and lysosome, respectively. Distribution of
222 endogenous EEA1 was dispersed into smaller puncta throughout the cytoplasm in ZIKV

infected WT cells, but not in ARF4$^{-/-}$ cells or mock infected cells where EEA1 accumulated as cytosolic foci at perinuclear regions **(Fig. 4g).** In contrast, distribution of lysosomes as detected by LAMP2 was expanded throughout the cytoplasm in ZIKV infected ARF4-deficient, but not in WT cells **(Fig. 4i).** Moreover, image analysis indicated that more ZIKV E proteins co-stained with EEA1 in WT cells, whereas E proteins were translocated and preferentially co-stained with LAMP-2 in ARF4$^{-/-}$ cells (**Fig. 4h and j**). These results demonstrated that ARF4-deficiency resulted in aberrant intracellular sorting and transport of virions, consequently triggering their lysosomal degradation instead of release.

ARF4 targeting peptides inhibit ARF4 activation, suppressing ZIKV infection.

Our subsequent focus was on exploration of ARF4 targeting peptides for their therapeutic efficacy against ZIKV infection. Previous studies have indicated that human rhodopsin regulates its intracellular trafficking by interacting with and activating endogenous ARF4 through its C-terminal motif, VXPX-COOH[26,27]. Therefore five peptides, named **ARF4 Targeting Peptides** 1-5 (ARF4TPs 1-5) basing on the VXPX sequence, were synthesized and characterized as detailed in **Fig. 5a**. Their 50% cytotoxicity concentration (CC_{50}) in Vero cells and the half maximal inhibitory concentration (IC_{50}) of ZIKV production were measured by MTT and RT-qPCR, respectively **(Fig. 5a and Extended Data Fig.16)**. ARF4TP-4 was identified as the most potent inhibitor against ZIKV, demonstrating an IC_{50} of 3.25 μM by RT-qPCR **(Fig. 5b)**, and 3.96 μM by plaque assay, serving as a measurement of infectivity of ZIKV progenies**(Fig. 5c)**. Additionally, ARF4TP-4 exhibited similar cytotoxicity and antiviral activity in HeLa cells. (**Extended Data 17).**

To elucidate the mechanism of ARF4TP-4 in ZIKV infection, we first investigated the stage(s) of infection affected by ARF4TP-4. F&T assay results showed ARF4TP-4 treatment did not impact the assembly and infectivity of viral particles. **(Extended Data Fig.18).** Similar to ARF4 deficiency, ARF4TP-4 treatment led to obvious reduction in RSP production in a dose dependent manner in Vero cells, and 20 μM of ARF4TP-4 completely abolished RSP production **(Fig. 5d-e)**. Subsequently, we explored the impact of ARF4TP-4 on the biological function of ARF4. Since GBF1 is required for ARF4 activation to form GBF1-ARF4 complex[28], we developed a model of ARF4TP-4 in complex with GBF1 and ARF4 by utilizing molecular docking. As illustrated in **Fig 5f**, ARFTP-4 binds to the groove composed by ARF4 and GBF1

with docking energy of -7.77 kcal/mol. To validate the docking result, the binding of human ARF4 and ARF4TP-4 was assessed through Surface Plasmon Resonance (SPR). ARF4TP-4 exhibited a binding affinity to recombinant human ARF4 protein with an estimated affinity constant (KD) of 3.96 μM **(Fig.5g-h).** Furthermore, VHS-GAT fused GST-pull down showed that ZIKV infection failed to activate ARF4 in the presence of high concentration of ARF4TP-4 (**Fig. 5i-k**). These findings collectively demonstrated that ARF4TP-4 inhibits ZIKV infection by competitively binding to host ARF4, thereby restraining the activation of ARF4.

Additionally, docking and SPR assay also showed a comparable binding affinity of ARF4TP-4 to ARF4 activated mutant-Q71I **(Extended Data Fig.19a-b).** We thus investigate the anti-ZIKV effect of ARF4TP-4 in WT ARF4 or ARF4-Q71I reconstituted in ARF4$^{-/-}$ cells. While the inhibition by ARF4TP-4 was rescued in WT ARF4 reconstituted ARF4$^{-/-}$ cells, ARF4TP-4 showed no anti-ZIKV activity in ARF4-Q71I reconstituted ARF4$^{-/-}$ cells, mirroring the results in parental ARF4$^{-/-}$ cells (**Extended Data Fig.19c**). In conclusion, our data demonstrate that competitive binding of ARF4TP-4 to endogenous ARF4 interferes with GBF1 stimulated activation, thereby blocking viral production.

ARF4TP-4 administration is safe and provides protection against ZIKV in mice.

Sequence alignment revealed a 96.11% identity between human and mouse ARF4 **(Extended Data Fig.20a)**. The analysis of the putative interaction between ARF4TP-4 and mouse ARF4 identified two amino acid substitutions (R73K and K79R) in the binding region. These substitutions possess properties similar to the human counterpart and therefore do not compromise the binding capability of ARF4TP-4. **(Extended Data Fig.20b).**

The safety and therapeutic efficacy of ARF4TP-4 in mice were initially assessed. Groups of C57BL/6 mice were intraperitoneally (IP) administered with ARF4TP-4 three times daily, with a dose escalation from 10 to 160 mg kg^{-1} of body weight **(Extended Data Fig.21a)**. Compared to the PBS vehicle group, ARF4TP-4 administration did not affect body weight nor induce any abnormal behaviour **(Extended Data Fig. 21b).** Additionally, the levels of alanine aminotransferase (ALT) **(Extended Data Fig. 21c)** and creatinine in sera **(Extended Data Fig. 21d),** indicative of hepatic and renal function, respectively, did not significantly change with ARF4TP-4 administration. Histopathological examination through Haematoxylin-and-eosin (HE) staining of brain, heart, liver, spleen, lung, kidney and testis sections revealed no pathological abnormalities regardless of PBS or ARFTP-4 treatments at various doses

(Extended Data Fig. 21e). ARF4TP-4 was thus deemed safe for mice, even at the highest dosage of 160 mg kg^{-1} of body weight.

Subsequently, to evaluate ARF4TP-4 as a potential antiviral agent, C57BL/6 mice were IP administered with ARF4TP-4 daily for three consecutive days. ZIKV challenge was conducted a day after the third ARF4TP-4 administration **(Fig. 5l).** ZIKV induced viremia was significantly reduced in ARF4TP-4 treated group compared to the vehicle group **(Fig. 5m).** Similar to the effect of ARF4 deletion, ARF4TP-4 treatment efficiently reduced the viral load and histopathological changes in both brain and testis **(Fig. 5n-o).**

ARF4 is a promising antiviral target with broad spectrum efficacy.

To ascertain the role of ARF4 in other RNA viruses, we extended our investigation to encompass several pathogenic RNA viruses, including IAV (H1N1), VSV, and SARS-CoV-2. Consistently, ARF4 abolishment significantly reduced the production of all tested viruses **(Fig. 6a).** Furthermore, to substantiate the *in vivo* relevance of ARF4, we established heterozygous ARF4 knock-out ($ARF4^{-/+}$) mice which exhibited a substantial reduction (> 60%) in ARF4 mRNA within the lung and trachea. **(Extended Data Fig. 22).** As shown in **Fig. 6b**, a lethal dose of IAV was intranasally administered into both $ARF4^{-/+}$ and WT control mice. Although both groups experienced body weight loss post IAV, $ARF4^{-/+}$ mice (6/8) exhibited weight recovery starting at 9 days p.i., with full recovery at 14 days p.i., consistent with WT mice (2/8) **(Extended Data Fig.23).** Survival analysis revealed a significant increase in survival rates, rising from 25% in control to 75% in $ARF4^{-/+}$ mice **(Fig. 6c).** Additionally, viral loads in trachea and lungs indicated remarkable reductions of nearly 90% and 70% respectively, in $ARF4^{-/+}$ mice **(Fig. 5d-e).** Notably, partial knock-out of ARF4 was sufficient to prevent typical IAV induced histopathological alterations, including alveolar septal thickening and fluid exudation in alveolar cavities, accompanied by inflammatory cell infiltration[29,30](**Fig. 6f-g**). Collectively, our findings underscore the crucial role of ARF4 in infection and pathogenesis of multiple RNA viruses.

IAV was then selected as a representative virus to evaluate the antiviral efficacy of ARF4TP-4. We firstly conducted an time-of-addition study including full time (FT) treatment, in which ARFTP-4 was sustained throughout the infection phase with additional 4hrs pre-

313 treatment, and post infection (PI) treatment which introduced ARF4TP-4 at 4 hrs p.i. **(Fig.**
314 **6h)**. Results showed that both FT and PI treatment exhibited dose-dependent suppression of
315 IAV infection, indicating the role of ARF4 also in the later stage of IAV infection. **(Fig. 6i).** We
316 then evaluated the *in vivo* efficacy of ARF4TP-4 against IAV challenge. C57BL/6 mice were
317 daily treated with varying doses of ARF4TP-4 four times upon IAV challenge, with PBS
318 serving as the control **(Fig. 6j).** Compared to control mice, ARF4TP-4 administration
319 demonstrated efficient protection from IAV induced weight loss. Particularly, in the high-
320 dose group (80 mg kg^{-1}) group, half of the mice presented no substantial weight loss post IAV
321 infection **(Extended Data Fig. 24).** Remarkably, ARF4TP-4 treatment conferred dose-
322 dependent protection, with a 44.4% survival rate in 20 mg kg^{-1} treated group, and up to a
323 75% in 80 mg kg^{-1} treated group **(Fig. 6k).** Consistent with findings in $ARF4^{-/+}$ mice, ARF4TP-4
324 treatment also efficiently blocked IAV infection in the trachea and lung while preserving
325 mice from lung histopathological alterations **(Fig. 6l-o)**. Importantly, viral load in the trachea
326 and lung was undetectable in some IAV-infected mice (3/6) from the 80mg kg^{-1} treatment
327 group, aligning with the observations on body weight**.** In conclusion, ARF4TP-4 showed
328 compelling pan antiviral capabilities, indicating its potential for further development.

329

330 **Discussion**

331 By utilizing ARF4-deficient cells and edited mice, we provide empirical evidence
332 revealing an essential role for the host factor ARF4 in infection and pathogenesis of multiple
333 RNA viruses, causing seasonal epidemics or worse global pandemics. We characterised ARF4
334 to show it functions in intracellular vesicle transport, playing an indispensable role in
335 determining transport and release of progeny virions. Furthermore, ARF4 activation was
336 confirmed to be essential for successful viral infection. Therefore, ARF4 targeting peptides
337 which efficiently blocked ARF4 activation suppressed viral infection both *in vitro* and *in vivo*,
338 preventing histopathological changes in viral-targeted tissues.

339 Vesicle transport between different intracellular organelles is the predominant way for
340 exchange of proteins and lipids in cells, as well as function in several fundamental biological
341 processes, like secretion and modification along secretory pathway.[31,32]. Vesicular trafficking

certainly plays an indispensable role in viral infectious life cycle especially for the final egress stage [33-35]. Here, the host factor-ARF4 was evidenced to be hijacked by multiple pathogenic RNA viruses to achieve a successful infection. Our studies confirm that ARF4 deletion or dysfunction by targeting peptides efficiently restricts the proliferation of highly pathogenic viruses, including ZIKV, IAV and newly emerged SARS-CoV-2. ARF4TP-4 also displays therapeutic effects in all tested infected mouse models. Therefore, ARF4-dependent characterization reveals a novel viral vulnerability which makes ARF4 as an attractive pan antiviral drug target.

Limited knowledge of intracellular vesicle transport and the mechanisms manipulated by viruses greatly impedes the development of antiviral therapies. Our results demonstrated that virus infection stimulates ARF4 activation, enabling appropriate sorting of progeny virions and regulating their intracellular vesicle transport for egress. Compared to Vero WT cells, ARF4 inactive mutant-T31N re-expressed in ARF4-deleted cells results in a nearly 2 log reduction, emphasizing the importance of ARF4 activation for successful viral infection. In contrast, a reduction of less than 1 log was evidence in ARF4 T31N overexpressing wild-type cells. These findings confirm endogenous ARF4 supports viral replication in ARF4 T31N overexpressing cells, albeit with attenuated function. These findings indicate that further investigations using a peptide targeted to block ARF4 activation should successfully suppress viral infection, relieve virus-induced pathogenic changes and reduce lethal death. Thus, therapeutic treatment aimed at regulation of ARF4 activation is a promising antiviral approach.

Considering the biological functions of host factors in their own cellular processes, potential toxicity is a main limitation of the development of antivirals targeting host factors[11,36-38]. Published reports indicate ARF4 functions with other ARFs, e.g. ARF1 or ARF5 in intracellular vesicle transport between the Golgi complex or along the early secretory pathway[39-41]. This indicates that ARF4 might not indispensable to the host. Thus, highly evolved, host adapted viruses hijack ARF4 to execute functions in the viral lifecycle, while coordinating with normal host cellular processes. Our experimental data support this hypothesis since ARF4 deletion did not induce toxicity in multiple virus-susceptible cells and gene-edited mice. Additionally, ARF4 targeting peptides exhibited minimal cytotoxicity and were safely administered in mice. ARF4 has been identified as essential for various

pathogenic RNA viruses excluding ZIKV. ARF4TP-4 has shown promising therapeutic efficacy against IAV infection in mice, highlighting its pan antiviral potential. A further understanding of how ARF4 modulates infection, and its involvement in the pathogenesis of other viruses, is necessary for the development of ARF4-targeted antivirals. Additionally, the effective delivery of antiviral peptides poses a big challenge due to the intracellular localization of ARF4[11,12,42]. Immunogenicity of peptides also need to be carefully considered since induced immune responses could potentially neutralize therapeutic peptides and lead to adverse host reactions [42,43].

Lastly, our data reveal that in ARF4-deleted cells, ZIKV progeny virions were mis-sorted into LE/MVBs surrounded by lysosome, initiating lysosomal degradation. Despite the absence of ARF4, viral egress is not completely arrested, suggesting some other unknown routes are also exploited. Recent research has uncovered several unconventional vesicle-dependent secretion pathways that are utilized by intracellular pathogens to escape circulating antibody and facilitate their dissemination. For instance, flaviviruses, like Dengue and ZIKV[24], as well as enteroviruses[44-46], such as polio, coxsackievirus B and enterovirus 71 were reported to egress via secretory autophagosomes which virion encapsulated autophagosomes are fused with cell membrane instead of lysosome. Our unpublished data indicate that a higher co-localization of viral E proteins with LC3-a marker of autophagy in ARF4$^{-/-}$ cells, implying a potential translocation of progeny virions into the autophagosomes for release when ARF4 is absent. Contrary to lysosomal degradation, β-Coronaviruses including SARS-CoV2 was reported to exploit lysosomes to initiate lysosomal trafficking for egress[47,48]. Therefore, lysosomes might be recruited for the secretion of progeny virions in ARF4 deficient cells.

Collectively, identification of ARF4 has revealed a vulnerability in infection by multiple pathogenic RNA viruses, providing a potential broad-spectrum antiviral targeting warranting further investigation to illustrate mechanisms for viral subversion.

Methods

Cells

Knockout ARF4 and ARF5 cells were generated using sgRNA sequences (ARF4: 5'-TCCCTCTTCTCCCGACTATT-3' and 5'- TATCCCTTACCTGGGTATTC-3' ; ARF5: 5'-GAAGATCCGCGAAAAGAGCG-3' and 5'- TGGACAGTAATGACCGGGAG-3') which cloned into the CRISPR/Ca9 vector pX459. Established clones were firstly transfected into Vero and HeLa cells respectively. Puromycin selection was performed after 48hrs transfection at a concentration of 10-12-10μg/ml in Vero and 1-2-1μg/ml in HeLa cells for 3 days. Single clones were picked by limiting dilution and confirmed by Western blotting using their specific antibodies . The stable cell lines expressing either prME-ZIKV or WT/mutants ARF4 were established using the retroviral vector pCHMES-IRES-Hygromycin, selected following a 2 week period in the presence of 500 μg/ml hygromycin in WT cells and half concentration in ARF4$^{-/-}$ cells. Single clones were picked by limiting dilution and confirmed by Western blotting using their specific antibodies. Selected positive clones were maintained thereafter in the same selection medium. Vero, HeLa and BHK21 based cells were maintained in DMEM supplemented with 10-15% fatal bovine serum (FBS) and 1% penicillin/streptomycin (P/S) at 37°C, with 5% CO_2. A549 cell was maintained in F-12K medium plus 10%FBS and 1% P/S at 37°C, with 5% CO_2. Aedes albopictus clone C6/36 was maintained in RPMI 1640 plus 15% FBS at 28°C, with 5% CO_2..

Viruses

ZIKV (strains NC-14-5132 and GZ01) was propagated in the C6/36 cells and titrated using plaque assay in Vero cells. Influenza A virus (A/WSN/33 H1N1) were grown and titrated using plaque assay in BHK21 cells. Recombinant VSV and SARS-CoV-2 (strain IME-BJ05) were propagated and titration using plaque assay in Vero cells. All experiments involving SARS-CoV-2 were performed in Biosafety level 3 facility in BIME, AMMS.

Antibodies

The following antibodies were used to detect ZIKV proteins: mouse anti-E mAb 4G2 (dilution 1:1000 for WB and 1:300 for IFA) from Novus Biologicals, or prepared using hybridoma cells D1-4G2-4-15 from ATCC; rabbit anti-E (GTX133325), rabbit anti-prM, as well as M (GTX133305),rabbit anti-capsid (GTX133317) from GeneTex as 1:500 dilution for WB. Rabbit anti-ARF4 (dilution 1:500 for WB and 1:300 for IFA) from Proteintech (11673-1-AP). Mouse anti-ARF5 mAb (1:200) from Abnova (H00000381-M01). Rabbit anti-Calnexin mAb (1:1000)

from cell signalling (2679) Mouse anti-Gapdh mAb (1:2000) from Abcam (ab8245). For immunofluorescence staining, following antibodies were used with 1:100 dilution as cellular markers: anti-GM130 (ab52649) anti-TGN46 (ab50595) and anti-LAMP2 (ab25631) from abcam;anti-EEA1 (3288) from cell signalling.

Mouse studies

All animal experimental procedures were carried out according to ethical guidelines and approval by Institutional Laboratory Animal Care and Use Committee at Beijing Institute of Microbiology and Epidemiology (IACUC-DWZX-2021-034 and IACUC-IME-2022-051). Gene-editing of mice were generated and bred by GemPharmatech Co. LTd. For ARF4 heterozygous knout out mice was also generated via CRISPR-Cas9 system. The brief process is as follows: sgRNA was transcribed in vitro.Cas9 and sgRNA were microinjected into the fertilized eggs of C57BL/6JGpt mice. Fertilized eggs were transplanted to obtain positive F0 mice which were confirmed by PCR and sequencing. A stable F1 generation mouse model was obtained by mating positive F0 generation mice with C57BL/6JGpt mice. For tissue specific knock-out mice: ARF4-flox/cre-Prok2 were established by utilizing Cre-LoxP system to firstly generate ARF4-flox and Cre-ProK2 C57BL/6JGpt mice via CRISPR-Cas9 system respectively, then the flox mice will be knock out after mating with mice expressing Cre recombinase, resulting in the loss of function of the target gene in specific tissues and cell types. For ARF4TP-4 efficiency assay, The specific pathogen-free wide-type C57BL/6JGpt mice were purchased at Beijing Vitalriver Laboratory Animal Technology Co. Ltd. In ZIKV challenge assay, either WT or gene-editing mice (4-6 weeks old) were IP administered with an anti-mouse IFNAR1 antibody (2mg/mice) a day before ZIKV challenge to suppress type I IFN responses. Then, $5*10^5$ PFU of ZIKV (GZ01) was infected i.p. To measure viral load, retro-orbitally bled and two main ZIKV targeting tissue- brain and testis were randomly collected from infected mice at indicated day post infection. 6 days post infected brain and testis were randomly collected to be fixed in 4% PFA for further HE staining. In IAV challenge assay, either WT or gene-editing mice (8-9 weeks old) were intranasally administrated with $1.5*10^4$ PFU. of IAV (A/WSN/33 H1N1). Body weight changes and mortality were monitored for 14 days. Lung and tracheal from 3 and 6 days p.i. were collected to check viral load. 6 days post infected lung were randomly collected to be fixed in 4% PFA, then sectioned and stained with haematoxylin and eosin (H&E).

Plaque assays to measure virus infection

Serial dilutions of SN from infected cells were added to BHK-21/Vero cell monolayer and adsorbed for 60 min at 37 C. Cells were washed and plaque media was overlaid on the cells and placed at 37 ℃. After 3-6 days of incubations, the cell monolayers were stained with crystal violet and plaques were counted.

Reverse transcription-quantitative PCR to measure viral RNA copies

Viral RNA was automatically extracted from viral infected mice sera or targeting tissue by GeneRotex 48 nucleic acid extractor (Tianlong) using viral DNA/RNA extraction kit. Then viral RNA copy numbers were amplified using the One Step PrimeScript RT-PCR kit (TaKaRa RR096a/RR064a). Primers in this study were designed using the Oligo software. ZIKV RNA copies were determined using a specific primer set (ZIKV-ASF: 5'-GGTCAGCGTCCTCTCTAATAAACG-3'; ZIKV-ASR: 5'-GCACCCTAGTGTCCACTTTTTCC-3'). IAV RNA copies were determined using a specific probe (5'-FAM TGCAGTCCTCGCTCACTGGGCACG-MGB-3') and primer set (QFluA-F: 5'-GACCRATCCTGTCACCTCTGAC-3'; QFluA-R: GGGCATTYTGGACAAAKCGTCTACG-3'). SARS-CoV-2 RNA copies were determined using a specific probe (5'- FAM- ACACTAGCCATCCTTACTGCGCTTCG -BHQ1-3') and primer set (gRNA-F 5'- ACAGGTACGTTAATAGTTAATAGCGT -3' and gRNA-R 5'- ATATTGCAGCAGTACGCACACA -3'). Following the manufacturer's protocol, 18 μl reaction mixtures of the One Step PrimeScript RT-PCR kit with 2 μl of RNA template were used to perform RT-qPCR assays using the LightCycler 480 real-time PCR system (Roche).

RSPs quantification

To identify RSPs secretion efficiency, RSPs producing cells were firstly replaced with FBS free culture medium for overnight starvation, subsequently, changed into OptiMEM without FBS or plus 2.5% FBS to initial RSPs production. After 1 or 2 days recovery of RSPs production, culture medium was collected and spin down at max speed, 2 min at 4 ℃ . Transparent culture medium was transferred into new tubes as supernatant (SN). Removing leftover culture medium, then washing with cold PBS 1-2 times. Cells were then lysed in cell lysis buffer and cell lysate (CL) was collected after centrifugation at max speed, 15min at 4 ℃. Collected SN and CL were added with 30ul 4× NuPAGE LDS sample buffer and subjected to western blotting assay using the specific antibody against ZIKV E proteins. The mean

luminescence and area of E protein signals detected in SN and CL were measured by densitometry using ImageJ software.

GST-VHS-GAT pull down assay

The activity of ARF4 was detected by GST-VHS-GAT pull down assay following the published protocol[15]. GST fused VHS-GAT was bacterially expressed and purchased from Sino Biological Inc. Pull down assay were performed by using Pierec™ GST protein interaction pull-down kit (Thermo Scientific). In brief, ZIKV or mock infected Vero cells with or without ARF4TP-4 treatment were lysed using pull-down lysis buffer provided by kit and measured by BCA protein assay kit (Thermo Scientific). 150μg GST-VHS-GAT was firstly incubated with 250μg cell lysate overnight at 4℃, and then added to equilibrate Glutathione Agarose column for additional overnight incubation at 4℃. After washing 1-2 times with 1ml washing solution, agarose slurry was resuspended by 85μl of 2× NuPAGE LDS sample buffe (Thermo Scientific) plus 10μl of 10*reducing buffer (Thermo Scientific) and 5μl 25*proteinase inhibitor. The bound proteins were then eluted and analysed by Western blotting with anti-ARF4 antibody.

Co-immunoprecipitation (Co-IP) assay

Sub-confluent ZIKV infected 10cm-diameter tissue culture plate Vero cells were lysed on ice or in a tube rotator at 4˚C for 30 min to 1hr with 1ml RIPA buffer [1% Triton X-100, 150 mM NaCl, 50 mM Tris-HCl, (pH 7.4), 1 mM EDTA0.5% (w/v) Na-deoxycholate supplemented with freshly added protease inhibitors cocktail(Roche)]. Cell debris were removed by centrifugation at 13,000 rpm for 15 min at 4˚C and cell lysates (CL) were pre-cleared by incubation with 30μl of 50% protein G Sepharose beads (GE Healthcare) for 1hr. Cleared CL were then overnight incubated with additional 60μl of 50% protein G Sepharose beads previously treated with specific antibodies. Beads were washed three times by pre-chilled wash buffer [0.1%Triton X-100, 50 mM Tris-Cl, pH 7.4, 300 mM NaCl, 5 mM EDTA, freshly adding 1* proteinase inhibitor cocktail (Roche)] and one time with cold PBS. Finally, beads were pelleted by centrifugation at 13,000 rpm for 30s at 4˚C and bound proteins were eluted by boiling in gel loading buffer, separated by electrophoresis and analysed with WB.

Transmission electron microscopy

Wild-type and ARF4$^{-/-}$ cells were infected with Zika (MOI 10, 24 h), fixed in 2.5% glutaraldehyde, washed three times in PBS and serially dehydrated. The cells were postfixed in 1% osmium tetroxide and embedded in Araldite resin (Polysciences). Blocks were sectioned with a diamond knife on an ultramicrotome (Leica microsystems) and examined with a transmission electron microscope (CM100, Philips).

Freeze-and-thaw assay

Sub-confluent ZIKV infected or RSPs-producing were firstly detached in PBS plus 5mM EDTA at 37°C for 5min, then washed with cold PBS of 5mM EDTA for three time. Cells finally were re-suspended in a buffer containing 10% w/v sucrose, 20mM Tris HCl, 150mM NaCl plus protease inhibitors cocktail (Roche), and then subjected to eight cycles of freeze (dry ice) and thaw (37°C water bath), 1min each step. Nuclei and cellular debris were removed by a short (5s) spin down at 14,000 RPM, 4°C. Supernatants were collected and centrifugated at 14,000 RPM, 4°C to pellet the membrane fraction which was then re-suspended in cold PBS. The final supernatant ,as cytosol fraction, containing newly formed ZIKV virions or RSPs, together with re-suspended membrane fraction, containing sole unpacked ZIKV E proteins, were analysed with western blotting assay using the specific antibody against ZIKV E proteins.

ssHRP quantification

Vero WT and ARF4$^{-/-}$ cells were transfected withpN1-HRP plasmid coding for a secreted form of the horseradish peroxidase (ss-HRP, a gift from Dr. Vivek Malhorta, Centre for Genomic Regulation, Barcelona, Spain). Culture medium was changed with fresh medium 48 h post-transfection and then collected 14 h later. To measure the activity of horseradish peroxidase, cleared supernatant was mixed with ECL Western blot detection reagent (Invitrogen), and luminescence intensity was then measured using the Microbeta luminometer (PerkinElmer Life Sciences).

Fluorescence microscopy

For fluorescence microscopy, cells grown on coverslips were fixed in 4% paraformaldehyde for 15 min, permeabilised with 0.1% TX-100 in PBS for 5 min and blocked with 5% goat serum 0.1% TX-100 in PBS for 30 min. Cells were incubated with primary antibodies for 2 h

at room temperature, and then probed with appropriate secondary antibodies. Nuclei were stained with DAPI and mounted on glass slides for image acquisition using LSM 700/780 confocal microscope. To determine ZIKV progeny virion or RSP localization in cellular sub-organelle, weighted co-localization coefficients of E with indicated cellular markers were computed using the ZEN2011 co-localization coefficient software (Carl Zeiss). The sums of intensities of pixels corresponding to co-staining with E and indicated cellular markers to anti-E (So) were computed and then weighted co-localization coefficients, which are equal to the ratio of Sc to So, were used to present the percentage of virions/RSP translocated to indicated sub-organelle.

RNA-sequencing and analysis

For RNA-sequencing assay, total RNAs were extracted from ZIKV or mock infected wild-type and ARF4-/- cells using TRIzol following manufacturer's protocols. RNA concentration and quality were assessed firstly before RNA-seq. The RNA library construction and high-throughput sequencing were performed by Beijing Annoroad Gene Technology Company. Briefly, multiplexed libraries were sequenced for 150 bp at both ends using an Illumina HiSeq6000 platform. Clean reads were aligned to the green monkey genome (Chlorocebus_sabeus 1.1) using Hisat2 (v2.1.0). The number of reads mapped to each gene in each sample was counted by HTSeq (v0.6.0) and FPKM (Fragments per Kilobase Million) was then calculated to estimate the expression level of genes in each sample. Genes with Padj < 0.05 and |Log2FC| ≥ 1 were identified as DEGs. DEGs were filtered by DESeq2 (v1.40.2) package in R (v4.3.1). GSEA(Gene Set Enrichment Analysis) of all genes and bubble chart were constructed using clusterProfiler (v4.8.3) package in R. Heatmaps of gene expression levels were constructed using heatmap (v1.0.12) package in R.

Biochemical fractionations assay

Mock- and virus-infected cells were pelleted and washed three times with PBS. Cells were homogenised in 10 mM Tris buffer (pH 7.2) containing 400 mM sucrose, 1 mM EDTA supplemented with protease inhibitor cocktail, using a loose pestle Dounce homogeniser. Homogenates were centrifuged at 100,000 × g for 45 min to collect total membranes or centrifuged sequentially at 1000 × g (10 min), 3000 × g (10 min), 25,000 × g (20 min) and 100,000 × g (30 min, Beckman TLA100.3 rotor) to collect membrane fractions. The 25,000 ×

g and 100,000 × g fractions were combined and resuspended in 750 µl of 1.25 M sucrose buffer and overlaid with 500 µl of 1.1 M and 500 µl of 0.25 M sucrose buffer. Centrifugation was performed at 120,000 × g for 2 h (Beckman TLS 55 rotor), after which the interface between 0.25 M and 1.1 M sucrose was collected and resuspended in 1 ml of 19% OptiPrep for a step gradient containing 0.5 ml 22.5%, 1 ml 19% (sample), 0.9 ml 16%, 0.9 ml 12%, 1 ml 8%, 0.5 ml 5% and 0.2 ml 0% OptiPrep each. The gradient was centrifuged at 150,000 × g for 3 h (Beckman SW 55 Ti rotor), and subsequently ten fractions, 0.5 ml each, were collected from the top.

Modelling human ARF4 and targeting peptide complexes

It has been reported that Arf4 and rhodopsin bind the regulatory N-terminal dimerization and cyclophilin-binding (DCB)-homology upstream of Sec7 (HUS) domain of GBF1[28]. To establish the models of human ARF4 in complex with GBF1 and ARF4 targeting peptide-ARF4TP-4, molecular docking was used. Firstly, the crystal structure of inactive human ARF4 (PDB ID: 1Z6X)[49] was downloaded from RCSB PDB Bank (http://www.rcsb.org). Secondly, the active human ARF4 was built based on a template from yeast ARF1 (PDB ID: 2KSQ). Thirdly, the AlphaFold-predicted structure of human GBF1 was downloaded from UniProt (UniProt ID: Q92538). Fourthly, the active ARF4-GBF1 complex structure was built based on a template Arf1-Brag2 complex (PDB ID: 4C0A). Fifthly, the active site of ARF4TP-4 was identified according to the previous study, in which α helix 3 of ARF4 was proposed as interacting partner of rhodopsin C terminus, the VXPX-COOH motif[50]. Finally, ARF4TP-4 were docked into the active site with AutoDockTools[51] and CUDA-accelerated AutoDock-GPU[52]. The 2D protein-ligand interaction were analysed by LigPlot+ (version 2.2.4)[53]. The 3D visualization and plot were generated by ChimeraX[54].

Surface Plasmon Resonance (SPR) assay

SPR technology-based binding assays were performed by Biacore T200 (Cytiva). Recombinant Human ARF4 WT was purchased from solarbio (P03581) and ARF4-Q71I mutant was made by SinoBiological. The activation reagent is prepared by mixing 400 mM EDC and 100 mM NHS (Cytiva) at a ratio of 1:1 immediately prior to injection. The CM5 sensor chip (Cytiva) is activated for 420s with the mixture at a flow rate of 10 µL/min. ARF4 WT or Q71I mutant protein were diluted to 20µg/ml in 10 mM sodium acetate (pH 4.5) and

inject them over the active channel surface to reach about 6900RU at 10μL/min. The chip is deactivated by 1 M Ethanolamine hydrochloride-NaOH (Cytiva) at a flow rate of 10 μL/min for 420s. Then, ARF4TP-4 was firstly diluted to 25μM in running buffer (1*PBS, with 0.05% Tween-20, pH7.4) and followed by a double concentration gradient dilution. Injected ARF4TP-4 for 60s over active and reference channels at 10 μL/min. The dissociation time is 60s. Finally, 1*PBST as regeneration buffer was injected for 30s at 30 μL/min to remove ARF4TP-4 from the surface. Select appropriate and continuous concentrations to perform kinetic 1:1 Binding or Steady-State analysis. The KD value representing the affinity constant was derived using Biacore T200 Evaluation software (Cytiva) and steady state analysis of data at equilibrium.

Cell cytotoxicity and antiviral inhibition of ARF4 targeting peptides (ARF4TPs)

ARF4TPs were synthesized by Nanjing TGpeptide Biotechnology Co. Ltd and dissolved in PBS to make a 10mM stock. To measure the 50% cytotoxic concentration (CC_{50}) of ARFTPs, the CellTiter-Glo® Cell Viability Assay (Promega) was employed to evaluate the cytotoxicity according to the manufacturer's protocols. In briefly, indicated cells were treated with different doses of either ARF4TPs or PBS in quadruplicate. Luminescence was recorded after 3 days of incubation and the CC_{50} was calculated using a sigmoidal nonlinear regression function to fit the dose-response curve using GraphPad Prism 7.0 software. To detect 50% inhibition concentration (IC_{50}), a serial diluted ARFTPs were added into overnight attached indicated cells. ZIKV infection was performed at a MOI of 0.1 after 4hrs ARF4TPs treatment and incubated 1hr at 37 °C. After incubation, infected cells were washed three time with PBS, then replenished with fresh culture medium plus indicated diluted ARF4TPs. Viral genomic RNA copy No. from 1 day p.i. supernatant were quantified by RT-qPCR with ZIKV specific primers and 50% IC_{50} was calculated as same method to IC50 using GraphPad Prism 7.0 software.

ARF4TP4 treatment assay *in vivo*

For ARFTP-4 safety experiment, C57BL/6 mice were assigned randomly to six groups and were injected by IP route with PBS (n=3), or ARF4TP-4 dissolved by PBS at escalating dose (10, 20, 40, 80 and 160 mg kg^{-1}, n=5) daily for three consecutive days. Body weight was measured daily after third ARF4TP-4 injection. Sera were collected at indicated days for ALT

and creatinine (CRE) detection by using the ALT assay kit and creatinine kit (NJJCBIO) respectively.. Two mice of each groups were sacrificed for tissue collection and following H&E staining. For ARF4TP-4 treatment upon ZIKV infection, 3-4 weeks C57BL/6 mice were assigned randomly to two groups and were injected by IP route with PBS, or 20mg kg^{-1} ARF4TP-4 daily for three consecutive days. ZIKV challenge were performed a day after first dose ARF4TP-4 injection. As an index of viremia, ZIKV genomic RNA in ZIKV infected mice sera were detected by RT-qPCR at 2, 4 and 6 days p.i.. Mice were sacrificed at indicated days p.i. for tissue collection for further detection. For ARF4TP-4 treatment upon IAV infection, 8-9 weeks C57BL/6 mice were assigned randomly to three groups and were injected by i.p. route with PBS, 20 mg kg^{-1} or 80 mg kg^{-1} ARF4TP-4. ARF4TP-4 as selected concentration were injected i.p. for four times. The first administration is a day before IAV challenge and others are conducted within the consecutive days post IAV intranasal inoculation. Body weight of infected mice was daily monitored till 15 days p.i. and percentage of body weight was measured as an index of IAV infection. Mice were sacrificed at day 3 and 6 p.i. for tissue collection and detection according to experimental demands.

Statistics and reproducibility

Statistical analyses were performed with GraphPad Prism software. In all figures, the datapoints and bar graphs represent the mean of independent biological replicates. In all graphs, the error bars represent the standard deviation and are only shown for experiments with n = 3 or greater as indicated. For microscopy experiments, data sets for quantitative analysis were acquired from an average of 40–50 fields from four to five independent reproducible experiments for each condition. Comparisons between control and sample datapoints were made using either the Student's unpaired t test, or two-way ANOVA with Dunnett's multiple-comparison analyses, or other statistics methods as specified in the figure legends with a confidence limit for significance set at 0.05 or less.

Reference

1 Guzman, M. G. *et al*. Dengue: a continuing global threat. *Nat Rev Microbiol* **8**, S7-16, doi:10.1038/nrmicro2460 (2010).

2 Lessler, J. *et al*. Assessing the global threat from Zika virus. *Science* **353**, aaf8160, doi:10.1126/science.aaf8160 (2016).

3 Eccleston-Turner, M., Phelan, A. & Katz, R. Preparing for the Next Pandemic - The WHO's Global Influenza Strategy. *The New England journal of medicine* **381**, 2192-2194, doi:10.1056/NEJMp1905224 (2019).
4 Wu, F. *et al.* A new coronavirus associated with human respiratory disease in China. *Nature* **579**, 265-269, doi:10.1038/s41586-020-2008-3 (2020).
5 Ventura, C. V., Maia, M., Bravo-Filho, V., Gois, A. L. & Belfort, R., Jr. Zika virus in Brazil and macular atrophy in a child with microcephaly. *Lancet* **387**, 228, doi:10.1016/S0140-6736(16)00006-4 (2016).
6 Shi, M. *et al.* The evolutionary history of vertebrate RNA viruses. *Nature* **556**, 197-202, doi:10.1038/s41586-018-0012-7 (2018).
7 Cui, J., Li, F. & Shi, Z. L. Origin and evolution of pathogenic coronaviruses. *Nature reviews. Microbiology* **17**, 181-192, doi:10.1038/s41579-018-0118-9 (2019).
8 Xiong, R. *et al.* Novel and potent inhibitors targeting DHODH are broad-spectrum antivirals against RNA viruses including newly-emerged coronavirus SARS-CoV-2. *Protein Cell* **11**, 723-739, doi:10.1007/s13238-020-00768-w (2020).
9 Kaur, H. *et al.* Efficacy and safety of dihydroorotate dehydrogenase (DHODH) inhibitors "leflunomide" and "teriflunomide" in Covid-19: A narrative review. *Eur J Pharmacol* **906**, 174233, doi:10.1016/j.ejphar.2021.174233 (2021).
10 Lin, K. & Gallay, P. Curing a viral infection by targeting the host: the example of cyclophilin inhibitors. *Antiviral research* **99**, 68-77, doi:10.1016/j.antiviral.2013.03.020 (2013).
11 Zumla, A., Chan, J. F., Azhar, E. I., Hui, D. S. & Yuen, K. Y. Coronaviruses - drug discovery and therapeutic options. *Nat Rev Drug Discov* **15**, 327-347, doi:10.1038/nrd.2015.37 (2016).
12 Li, G., Hilgenfeld, R., Whitley, R. & De Clercq, E. Therapeutic strategies for COVID-19: progress and lessons learned. *Nat Rev Drug Discov* **22**, 449-475, doi:10.1038/s41573-023-00672-y (2023).
13 Shie, J. J. & Fang, J. M. Development of effective anti-influenza drugs: congeners and conjugates - a review. *J Biomed Sci* **26**, 84, doi:10.1186/s12929-019-0567-0 (2019).
14 Donaldson, J. G. & Jackson, C. L. ARF family G proteins and their regulators: roles in membrane transport, development and disease. *Nat Rev Mol Cell Biol* **12**, 362-375, doi:10.1038/nrm3117 (2011).
15 Cohen, L. A. & Donaldson, J. G. Analysis of Arf GTP-binding protein function in cells. *Curr Protoc Cell Biol* **Chapter 3**, Unit 14 12 11-17, doi:10.1002/0471143030.cb1412s48 (2010).
16 Verheije, M. H. *et al.* Mouse hepatitis coronavirus RNA replication depends on GBF1-mediated ARF1 activation. *PLoS Pathog* **4**, e1000088, doi:10.1371/journal.ppat.1000088 (2008).
17 Dorobantu, C. M. *et al.* Recruitment of PI4KIIIbeta to coxsackievirus B3 replication organelles is independent of ACBD3, GBF1, and Arf1. *Journal of virology* **88**, 2725-2736, doi:10.1128/JVI.03650-13 (2014).
18 Wang, P. G. *et al.* Efficient assembly and secretion of recombinant subviral particles of the four dengue serotypes using native prM and E proteins. *PLoS One* **4**, e8325, doi:10.1371/journal.pone.0008325 (2009).
19 Kudelko, M. *et al.* Class II ADP-ribosylation Factors Are Required for Efficient Secretion of Dengue Viruses. *J Biol Chem* **287**, 767-777, doi:M111.270579 [pii]10.1074/jbc.M111.270579 (2012).

20 Lee, C. Y. *et al*. Type I interferon shapes the quantity and quality of the anti-Zika virus antibody response. *Clin Transl Immunology* **9**, e1126, doi:10.1002/cti2.1126 (2020).
21 Boman, A. L., Zhang, C., Zhu, X. & Kahn, R. A. A family of ADP-ribosylation factor effectors that can alter membrane transport through the trans-Golgi. *Mol Biol Cell* **11**, 1241-1255, doi:10.1091/mbc.11.4.1241 (2000).
22 Dell'Angelica, E. C. *et al*. GGAs: a family of ADP ribosylation factor-binding proteins related to adaptors and associated with the Golgi complex. *J Cell Biol* **149**, 81-94, doi:10.1083/jcb.149.1.81 (2000).
23 Lan, Y. *et al*. Viral subversion of selective autophagy is critical for biogenesis of virus replication organelles. *Nat Commun* **14**, 2698, doi:10.1038/s41467-023-38377-w (2023).
24 Li, M. Y. *et al*. Lyn kinase regulates egress of flaviviruses in autophagosome-derived organelles. *Nat Commun* **11**, 5189, doi:10.1038/s41467-020-19028-w (2020).
25 Li, M. Y. *et al*. KDEL Receptors Assist Dengue Virus Exit from the Endoplasmic Reticulum. *Cell reports*, doi:10.1016/j.celrep.2015.02.021 (2015).
26 Deretic, D. *et al*. Rhodopsin C terminus, the site of mutations causing retinal disease, regulates trafficking by binding to ADP-ribosylation factor 4 (ARF4). *Proc Natl Acad Sci U S A* **102**, 3301-3306, doi:10.1073/pnas.0500095102 (2005).
27 Mazelova, J. *et al*. Ciliary targeting motif VxPx directs assembly of a trafficking module through Arf4. *The EMBO journal* **28**, 183-192, doi:10.1038/emboj.2008.267 (2009).
28 Wang, J., Fresquez, T., Kandachar, V. & Deretic, D. The Arf GEF GBF1 and Arf4 synergize with the sensory receptor cargo, rhodopsin, to regulate ciliary membrane trafficking. *Journal of cell science* **130**, 3975-3987, doi:10.1242/jcs.205492 (2017).
29 Thangavel, R. R. & Bouvier, N. M. Animal models for influenza virus pathogenesis, transmission, and immunology. *J Immunol Methods* **410**, 60-79, doi:10.1016/j.jim.2014.03.023 (2014).
30 Bouvier, N. M. & Lowen, A. C. Animal Models for Influenza Virus Pathogenesis and Transmission. *Viruses* **2**, 1530-1563, doi:10.3390/v20801530 (2010).
31 Bonifacino, J. S. & Glick, B. S. The mechanisms of vesicle budding and fusion. *Cell* **116**, 153-166, doi:10.1016/s0092-8674(03)01079-1 (2004).
32 Mellman, I. & Warren, G. The road taken: past and future foundations of membrane traffic. *Cell* **100**, 99-112, doi:10.1016/s0092-8674(00)81687-6 (2000).
33 Roth, A. N. *et al*. Ins and Outs of Reovirus: Vesicular Trafficking in Viral Entry and Egress. *Trends in microbiology* **29**, 363-375, doi:10.1016/j.tim.2020.09.004 (2021).
34 Hassan, Z., Kumar, N. D., Reggiori, F. & Khan, G. How Viruses Hijack and Modify the Secretory Transport Pathway. *Cells* **10**, doi:10.3390/cells10102535 (2021).
35 Coller, K. E. *et al*. Molecular determinants and dynamics of hepatitis C virus secretion. *PLoS Pathog* **8**, e1002466, doi:10.1371/journal.ppat.1002466 (2012).
36 zur Wiesch, P. A., Kouyos, R., Engelstadter, J., Regoes, R. R. & Bonhoeffer, S. Population biological principles of drug-resistance evolution in infectious diseases. *The Lancet. Infectious diseases* **11**, 236-247, doi:10.1016/S1473-3099(10)70264-4 (2011).
37 Li, G., Hilgenfeld, R., Whitley, R. & De Clercq, E. Therapeutic strategies for COVID-19: progress and lessons learned. *Nat Rev Drug Discov*, 1-27, doi:10.1038/s41573-023-00672-y (2023).

38 Barrows, N. J. *et al*. A Screen of FDA-Approved Drugs for Inhibitors of Zika Virus Infection. *Cell Host Microbe* **20**, 259-270, doi:10.1016/j.chom.2016.07.004 (2016).
39 Chun, J., Shapovalova, Z., Dejgaard, S. Y., Presley, J. F. & Melancon, P. Characterization of class I and II ADP-ribosylation factors (Arfs) in live cells: GDP-bound class II Arfs associate with the ER-Golgi intermediate compartment independently of GBF1. *Mol Biol Cell* **19**, 3488-3500, doi:10.1091/mbc.E08-04-0373 (2008).
40 Duijsings, D. *et al*. Differential membrane association properties and regulation of class I and class II Arfs. *Traffic* **10**, 316-323, doi:10.1111/j.1600-0854.2008.00868.x (2009).
41 BuNakai, W. *et al*. ARF1 and ARF4 regulate recycling endosomal morphology and retrograde transport from endosomes to the Golgi apparatus. *Mol Biol Cell* **24**, 2570-2581, doi:10.1091/mbc.E13-04-0197 (2013).
42 Lu, L., Su, S., Yang, H. & Jiang, S. Antivirals with common targets against highly pathogenic viruses. *Cell* **184**, 1604-1620, doi:10.1016/j.cell.2021.02.013 (2021).
43 Fernandez, L. *et al*. Immunogenicity in Protein and Peptide Based-Therapeutics: An Overview. *Curr Protein Pept Sci* **19**, 958-971, doi:10.2174/1389203718666170828123449 (2018).
44 Robinson, S. M. *et al*. Coxsackievirus B exits the host cell in shed microvesicles displaying autophagosomal markers. *PLoS Pathog* **10**, e1004045, doi:10.1371/journal.ppat.1004045 (2014).
45 Chen, Y. H. *et al*. Phosphatidylserine vesicles enable efficient en bloc transmission of enteroviruses. *Cell* **160**, 619-630, doi:10.1016/j.cell.2015.01.032 (2015).
46 Mutsafi, Y. & Altan-Bonnet, N. Enterovirus Transmission by Secretory Autophagy. *Viruses* **10**, doi:10.3390/v10030139 (2018).
47 Ghosh, S. *et al*. beta-Coronaviruses Use Lysosomes for Egress Instead of the Biosynthetic Secretory Pathway. *Cell* **183**, 1520-1535 e1514, doi:10.1016/j.cell.2020.10.039 (2020).
48 Xia, B. *et al*. Extracellular vesicles mediate antibody-resistant transmission of SARS-CoV-2. *Cell Discov* **9**, 2, doi:10.1038/s41421-022-00510-2 (2023).
49 Zhao, Y. *et al*. Cryo-EM structures of apo and antagonist-bound human Cav3.1. *Nature* **576**, 492-497, doi:10.1038/s41586-019-1801-3 (2019).
50 Deretic, D. *et al*. Rhodopsin C terminus, the site of mutations causing retinal disease, regulates trafficking by binding to ADP-ribosylation factor 4 (ARF4). *Proceedings of the National Academy of Sciences* **102**, 3301-3306, doi:doi:10.1073/pnas.0500095102 (2005).
51 Morris, G. M. *et al*. AutoDock4 and AutoDockTools4: Automated Docking with Selective Receptor Flexibility. *J Comput Chem* **30**, 2785-2791, doi:10.1002/jcc.21256 (2009).
52 Santos-Martins, D. *et al*. Accelerating AutoDock4 with GPUs and Gradient-Based Local Search. *J Chem Theory Comput* **17**, 1060-1073, doi:10.1021/acs.jctc.0c01006 (2021).
53 Laskowski, R. A. & Swindells, M. B. LigPlot+: Multiple Ligand–Protein Interaction Diagrams for Drug Discovery. *Journal of chemical information and modeling* **51**, 2778-2786, doi:10.1021/ci200227u (2011).

54 Pettersen, E. F. *et al.* UCSF ChimeraX: Structure visualization for researchers, educators, and developers. *Protein Science* **30**, 70-82, doi:https://doi.org/10.1002/pro.3943 (2021).

Acknowledgement

We thank Prof. Lu Lu for help in discussion and critical reagents. This study was supported by the National Key Research and Development Project of China (2022YFC2303700), the National Natural Science Foundation of China (82172271) to M.Y.L. and State Key Laboratory of Pathogen and Biosecurity (SKLPBS2019). P.H.C. was supported by the University Grants Committee's Collaborative Research Fund (C6036-21G), General Research Fund (16301319). Y.Q.D was supported by the Key-Area Research and Development Program of Guangdong Province (2022B1111020002). Works in T.T.L lab is supported by grants from InnoHK, an initiative of the Innovation and Technology Commission, the Government of the Hong Kong Special Administrative Region. Works in the S.S lab is supported by the Welcome Trust (220776/Z/20/Z and 223107/Z/21/Z to SS and 225010/Z/22/Z to VS). C.F.Q. was supported by the National Science Fund for Distinguished Young Scholar (81925025) and the Innovation Fund for Medical Sciences (2019-I2M-5-049) from the Chinese Academy of Medical Sciences.

Author contributions

C.F.Q., S.S. and M.Y.L. conceived the study and wrote the manuscript. M.Y.L., K.D., X.H.C., L.Y.L.S., T.S.N., V.G.S., Q.W.T., S.V.L., H.H.W., Y.L., T.T.L, M.X.S, N.N.Z., Y.Z., T.S.C., F.Y., and Y.Q.D. conducted and analyzed the experiments. P.P.H.C., Z.R.G. performed transcriptome profiles analysis. All authors reviewed and approved the manuscript.

Competing interests

C.F.Q. and M.Y.L. have filed a patent related to the finding reported in this paper.

Main figure titles and legends

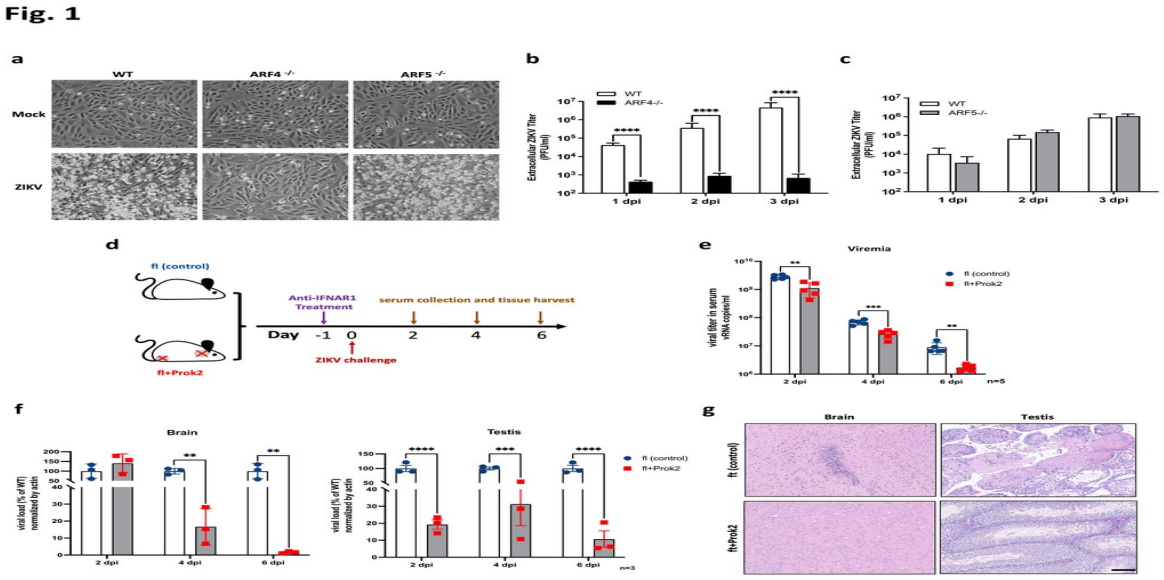

Fig. 1 ARF4 facilitates ZIKV infection and leads to pathogenesis. a-c) ARF4$^{-/-}$, ARF5$^{-/-}$ and WT Vero cells were challenged with ZIKV at MOI of 0.1. Culture medium was collected daily until cytopathic effects were observed in WT cells which appeared at day 3 days post infection (dpi) shown in a). Viral titres were determined by plaque assay on Vero cells and expressed as PFU/ml. **d)** Schematic of ARF4-flox [fl(control)] and ARF4 brain/testis-specific knock-out (ft+Prok2) mice with ZIKV challenge and detection. **e-f)** Serum, brain and testis were collected from ZIKV infected fl+ProK2 and fl (control) mice at indicated dpi. Total RNA was extracted as a template to calculate viral load by performing RT-qPCR. **h)** ZIKV-infected brains and testis were collected and fixed at 6 dpi, then stained with haematoxylin and eosin (H&E) and examined by light microscopy observation. Data are shown as mean ± SD **P<0.01, ***P<0.001 and ****P<0.0001 vs WT or fl (control) by two-way ANOVA with multiple comparisons. H&E images are representative of three mice. Scale bar, 100 μm.

Fig. 2

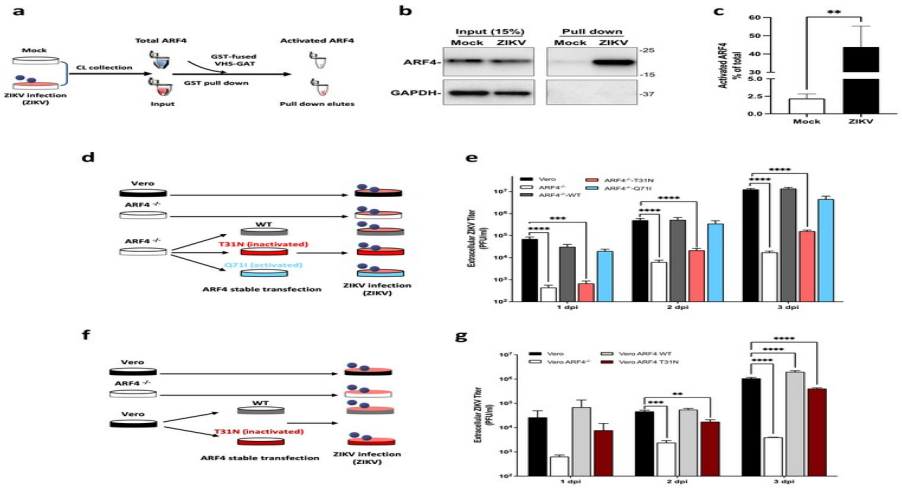

Fig. 2 ARF4 activation during ZIKV infection is essential for producing progeny virions. a) Schematic of ARF4 activation detection by VHS-GAT fused GST pull down. **b-c)** Cell lysates (CL) were collected from mock or ZIKV infected (MOI=5, 30 hrs) to perform GST pull down using GST fused VHS-GAT bait. CL and final eluates, serving as input and pull down respectively, were subjected to WB by antibody against ARF4 and GAPDH as loading control. The activity of ARF4 was calculated as the percentage of activated ARF4 in final eluates relative to total ARF4 in CL. Data are shown as mean ± SD **P<0.05 vs mock infection by Student's unpaired t test. **d)** Schematic of ARF4 stable transfection in Vero ARF4$^{-/-}$ cells and ZIKV infection. **e)** ZIKV infection was performed in Vero, ARF4$^{-/-}$ and reconstituted cells (MOI=0.1). Supernatant (SN) were daily collection for 3 days p.i. for viral titration by plaque assay. **f-g)** Vero cells stably overexpressing WT and T31N ARF4 were established and infected with ZIKV (MOI=0.1). Viral titres were detected by plaque assay. Results in e) and f) are presented as means ±SD. **P<0.01,***P<0.001, ****P<0.0001 Versus Vero (same collection day) by two-way ANOVA with multiple comparisons.

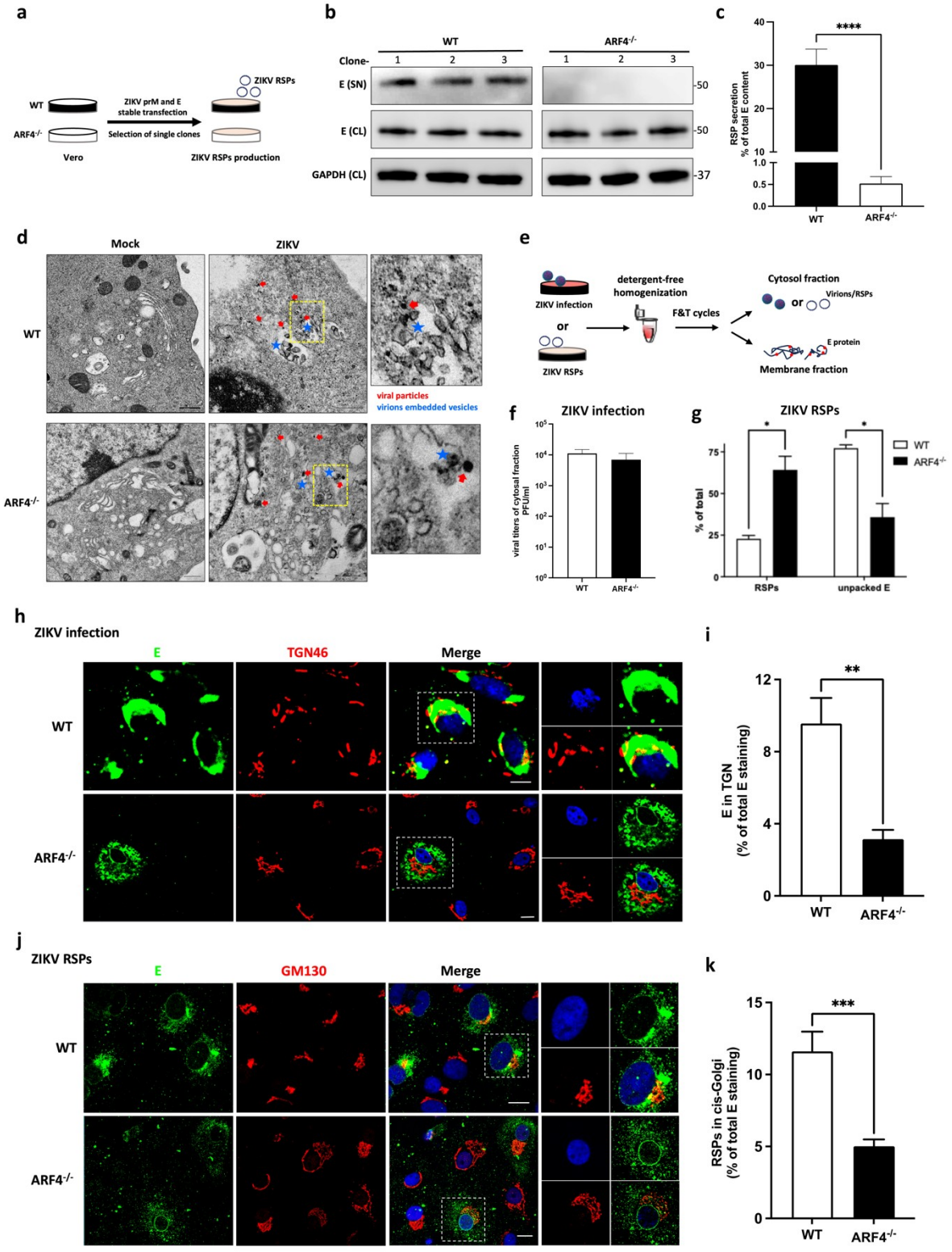

865

866 **Fig. 3 ARF4 is essential for intracellular transport and egress of ZIKV. a)** Schematic of
867 generating cells stably producing ZIKV recombinant subviral particles (RSPs). **b-c)** Single
868 clones (-1, 2 and 3) of either Vero WT-ZIKV prME or Vero ARF4$^{-/-}$ -ZIKV prME were isolated

and maintained separately. Supernatants (SN) and cell lysates (CL) were collected to perform WB. E protein was detected using a specific antibody. GAPDH served as a loading control. Percentage of E(SN) in total E(SN+CL) was measured as an index of RSP secretion. **d)** ZIKV infection was performed in Vero WT and ARF4$^{-/-}$cells (MOI=10, 24 hrs. Cells were fixed and viral particles were visualized by transmission electron microscopy (TEM). Newly formed virions are indicated by red arrows and ER invaginations containing viral particles are indicated by blue stars. Scale bar, 500 nm **e)** Schematic of isolating intracellular ZIKV virion/RSPs and unpacked viral E protein by Freeze-and-thaw (F&T) assay. **f)** Vero WT and ARF4-/- cells were infected by ZIKV (MOI=5, 30 hrs) to perform F&T assay. Titration of infectious virions in isolated cytosol fractions was performed by plaque assay. **g)** F&T assay was performed in ZIKV RSP producing Vero WT and ARF4$^{-/-}$ cells. E protein was detected in isolated cytosol and membrane fraction as an index of formed RSPs and unpacked membrane viral protein respectively. Percentage of E measured from cytosol fraction relative to the total amount (cytosol+membrane) was used as an index of RSP formation. Unpacked E from membrane fraction was presented as percentage of E from membrane fraction relative to the total input amount. **h-k)** Viral E protein was co-stained with TGN46 (trans-Golgi network (TGN) marker) or GM130 (cis-Golgi marker) by their specific antibodies in ZIKV infected Vero cells (MOI=10, 36 hrs)(g) or RSP-producing cells (I). Scale bar=10 μM. The percentage of E protein in TGN or cis-Golgi is presented as the weighted co-localization coefficients of E staining in TGN46 or GM130 stained areas by using imaging analysis software-ZEN2012 (Carl Zeiss) from >100 cells per condition. TEM and IFA images are representative of at least three independent experiments. Results are presented as means ±SD *P<0.05, **P<0.01, ***P<0.001 and ****P<0.0001 versus untreated control or WT by the Student's unpaired t test or two-way ANOVA with multiple comparisons.

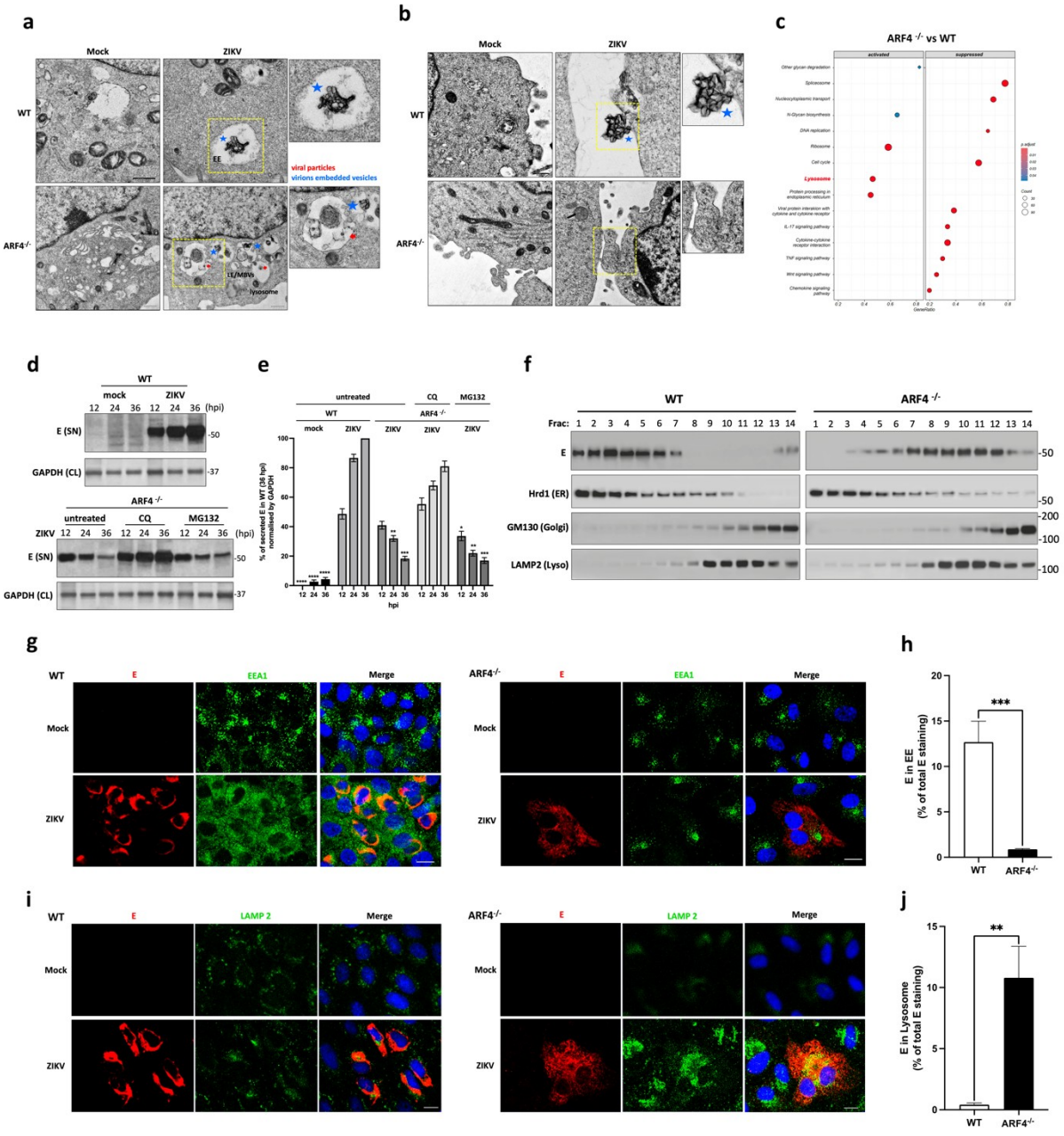

893

894 **Fig. 4 ARF4-deficiency causes mis-sorting of newly formed viral particles into the lysosomal**
895 **degradation pathway. a-b)** TEM observation was performed with the same cells as
896 described above. Virion-containing vesicles are indicated by blue stars . Dispersed unpacked
897 virions are indicated by red arrows. Sub-cellular organelles - early endosome (LL), late
898 endosome (LE) or multivesicular body (MVBs)-like compartments in figure a, as well as
899 membrane protrusions in figure b are highlighted by yellow boxes. Scale bar, 500nm. **c)** Total
900 RNA extracted from ZIKV infected Vero WT and ARF4$^{-/-}$ cells (MOI=0.1 48hrs) was used for
901 RNA-seq. Bubble chart shows the GSEA analysis results, indicating that the lysosomal

902 pathway is activated in ARF4 knockout group compared to WT group. **d)** Vero WT were mock
903 or ZIKV infected with MOI of 2. ARF4-/- cells were treated overnight with chloroquine CQ (20
904 µM) and MG132 (50 µM) and then infected by ZIKV(MOI=2). Cells were radioactively
905 labelled ([35S]cysteine/methionine) after infection. Supernatants were collected at indicated
906 time for autoradiography. GAPDH in CL served as loading control. **e)** Quantitative
907 densitometry data of the released E proteins in supernatant (SN) were normalized to their
908 respective loading control. Results are displayed as the percentage of E from selected
909 samples relative to E from WT cell at 36hrs post ZIKV infection. Results are means ±SD
910 *P<0.05, **P<0.01, ***P<0.001 and ****P<0.0001 versus untreated ZIKV infected WT (same
911 collected time) by two-way ANOVA with multiple comparisons. **f)** Vero WT and ARF4$^{-/-}$ cells
912 were infected by ZIKV at MOI of 2. Infected cells were collected at 48hrs p.i. for biochemical
913 fractionation to isolate intracellular compartments of the secretory/endolysosomal
914 compartments. The intracellular distribution of progeny ZIKV virions or E proteins were
915 detected by WB using antibodies against E and indicated organelle markers. **g-j)** Vero WT
916 and ARF4$^{-/-}$ cells were mock or ZIKV infected (MOI=10, 24 hrs). Cells were then fixed and co-
917 stained with antibodies against viral E, along with EEA1 (g), or LAMP2 (i). Nuclei were stained
918 with DAPI. Scale bar =10 µM. Selected images are representative of at least three
919 independent experiments. The percentage of E protein in EE or lysosome was presented as
920 the weighted co-localization coefficients of E staining in EEA1 or LAMP2 stained areas,
921 analysed using ZEN2012 (Carl Zeiss) imaging software from >100 cells per condition. Results
922 are means ±SD **P<0.01, and ***P<0.001 versus WT by the Student's unpaired t test.

Fig. 5

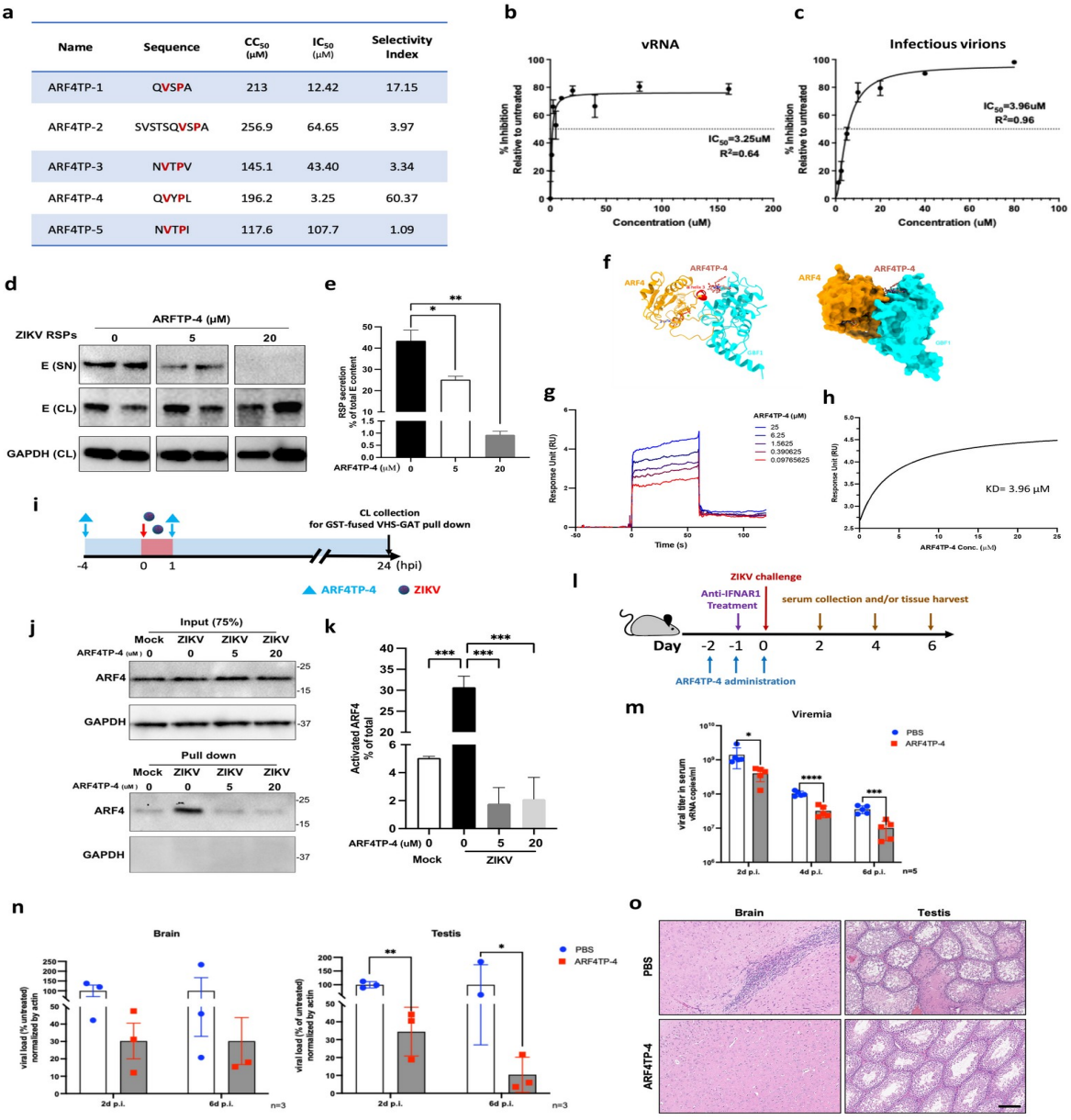

923

924 **Fig. 5 ARF4TP-4 peptide interferes with ARF4 activation and arrests viral infection both *in***
925 ***vitro* and *in vivo*. a)** CC_{50} and IC_{50} of ARF4 targeting peptides named ARF4TPs was measured
926 as described in the methods section. **b-c)** IC_{50} curves showing the effect of ARF4TP-4 on the
927 inhibition of ZIKV viral genomic RNA (b) and infectious progeny virions (c). **d-e)** Vero-ZIKV
928 prME cells were treated with ARF4TP-4 at indicated concentrations. SN and CL were
929 collected to perform WB to detect RSP secretion. RSPs secretion was calculated as described

above. **f)** 3D visualization of putative interaction between ARF4TP-4 and human ARF4. ARF4 is rendered as a cartoon and coloured orange, with the red-highlighted α-helix 3 proposed as the interacting partner of ARFTP-4. GBF1 is rendered as a cartoon and coloured in cyan. The peptide QVYPL is rendered as a ball-stick model and coloured in salmon. The surface plot of ARF4, ARF4TP-4 and GBF1 complex is shown on the right. **g-h)** The binding of ARF4TP-4 to human ARF4 was measured by SPR. Graphs of equilibrium response units versus compound concentrations are plotted. The estimated affinity constant (KD) is 3.96 μM. **i)** Schematic of ARF4TP-4 treatment and ZIKV challenge for ARF4 activation detection. **j-k)** ARF4 activity was detected and measured by performing GST-VHS-GAT pull down as described in the methods section. Data are shown as mean ± SD ***P<0.001 by two-way ANOVA. **l)** Schematic of ARFTP-4 treatment in ZIKV-infected mice. **m-o)** Viremia, viral load and histopathological changes in brain and testis were tested following similar processes described in Fig 1. Results are shown as means ± SD *P<0.05, **P<0.01, ***P<0.001 and ****P<0.0001 versus PBS control by two-way ANOVA with multiple comparisons. Selected H&E staining images are representative of three randomly selected mice. Scale bar, 100 μM.

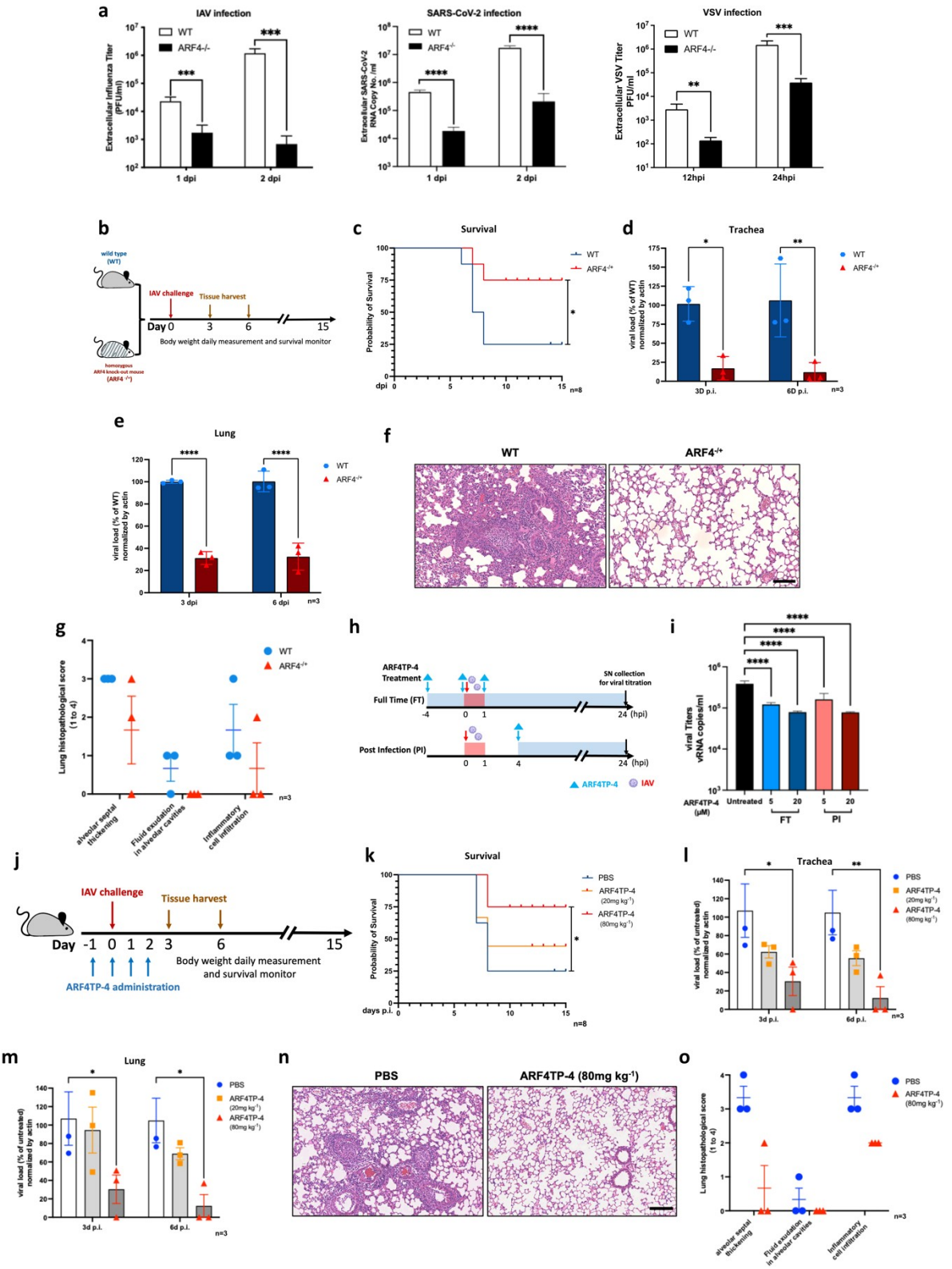

945

946 **Fig. 6 ARF4 deficiency or dysfunction impedes infection and histopathological changes of**
947 **pathogenic RNA viruses. a)** IAV (H1N1) (MOI=1), SARS-CoV-2 (MOI=0.01) and VSV
948 (MOI=0.01) were used to infect Vero WT and ARF4$^{-/-}$ cells. Viral titres of IAV and VSV were

949 measured by plaque assay as PFU/ml. Viral genomic RNA of SARS-CoV-2 was calculated by
950 RT-qPCR as RNA copy no./ml. **b)** Schematic of IAV challenge and detection in WT and ARF4$^{-/+}$
951 mice. **c)** Survival rate was assessed to create a survival curve by using Prism software.
952 *P<0.05 vs WT by Long-rank (Mantel-Cox) test. **d-e)** Viral load of lung and trachea at
953 indicated days p.i. were calculated by RT-qPCR using IAV-specific probe and primers. **f-g)** H&E
954 staining and histopathological score of IAV infected lung sections collected from WT and
955 ARF4$^{-/+}$ mice at 6 dpi. **h-i)** Vero cells were treated with ARF4TP-4 and infected by IAV
956 (MOI=0.5) as described in the schematic. SN was collected for viral titration by RT-qPCR. Data
957 are shown as mean ± SD ****P<0.0001 vs untreated control by two-way ANOVA with
958 multiple comparisons. **j)** Schematic of ARF4TP-4 treatment in IAV infection in vivo. **k-o)**
959 Survival curve, viral load and histopathological changes in lung were tested respectively
960 following similar methods described above. Results are shown as means ± SD *P<0.05,
961 **P<0.01, ***P<0.001 and ****P<0.0001 vs PBS control by two-way ANOVA with multiple
962 comparisons. Selected H&E staining images are representative of three randomly selected
963 mice. Scale bar,100 μM.

Extended Data figure titles and legends

Extended Data Fig.1 ARF4 or ARF5 deletetion in Vero cells by CRISPR-Cas9 gene-editing (ARF4$^{-/-}$ and ARF5$^{-/-}$). Cell lysates (CL) from knockout and wild type (WT) cells were collected to verify deletion efficiency by Western blotting (WB) using ARF4 and ARF5 specified antibodies. GAPDH was used as loading control.

Extended Data Fig.2 ZIKV infection is inhibited in ARF4-deleted HeLa cells. a) CL from WT and ARF4$^{-/-}$ HeLa cells were collected to verify deletion efficiency by WB with anti-ARF4 antibody. GAPDH was used as loading control. **b)** ARF4$^{-/-}$ and WT HeLa cells were challenged with ZIKV at MOI of 0.1. Culture medium was collected daily until cytopathic effects were observed in WT cells which appeared at day 3 days post infection (dpi). Viral titres were determined by plaque assay on Vero cells and expressed as PFU/ml.

Extended Data Fig.3 Transcription of ARF4, not ARF5 is reduced in brain and testis of fl+Prok mice. C57BL/6JGpt based control ARF4-flox [fl(control)] and knockout ARF4-flox/cre-Prok2 (fl+Prok) mice were generated and then collected for transcription measurement. Total RNA were isolated from indicated viral targeting tissues to be used as templates for the following RT-qPCR using ARF4 and ARF5 specific primers respectively. The data are shown as mean ± SD ***P<0.001 and ****P<0.0001 vs ft control by two-way ANOVA with multiple comparisons.

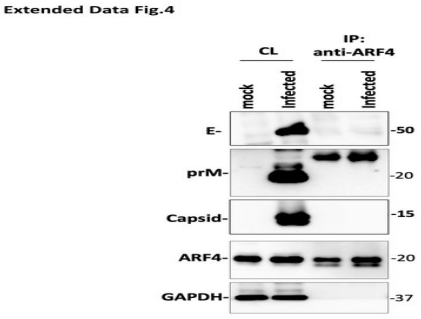

Extended Data Fig.4 ZIKV structural proteins do not bind to endogenous ARF4. CL from ZIKV infected Vero cells (MOI=5, 48hrs) were collected to perform immunoprecipitation (IP) assay using anti-ARF4 antibody to pull down endogenous ARF4. IP eluates were subject to WB using antibodies against viral E, prM and capsid proteins, as well as the host ARF4 protein. GAPDH was used as loading control.

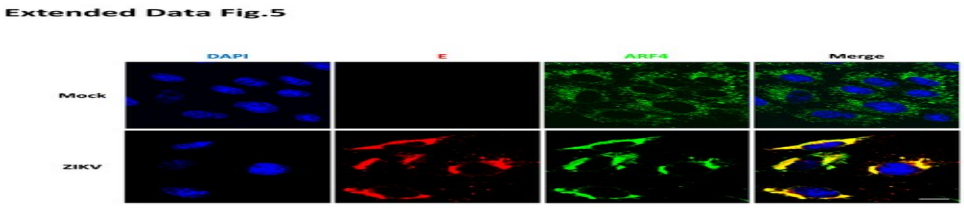

Extended Data Fig.5 Endogenous ARF4 is re-distributed upon ZIKV infection. Vero cells were mock or ZIKV infected with MOI of 10 and fixed at 36hrs post infection. Viral E protein was co-stained with endogenous ARF4 using their specific antibodies. Scale bar=10μM.

Extended Data Fig.6 Generation of cells stably expressing ARF4 mutants. a) WT ARF4 or its constitutively inactive mutant (T31N) or active mutant (Q71I) were reconstituted and stably expressed in ARF4 $^{-/-}$ cells. **b)** WT and T31N ARF4 were stably overexpressed in Vero cells. CL from a and b were collected to perform WB using anti-ARF4 antibody. GAPDH is used as loading control.

Extended Data Fig.7 ARF4 does not affect ZIKV intracellular infection. a) Vero WT and ARF4$^{-/-}$ cells were infected by ZIKV (MOI=0.1) and collected at 1-3 dpi respectively. Total RNA extracted from collected cells were used as templates to perform RT-qPCR assay using ZIKV-specific primers. Viral RNA (vRNA) was calculated as vRNA copy No./ml. **b-c)** Intracellular vRNA was calculated in ZIKV-infected cells expressing ARF4 mutants (MOI=0.1 1dpi) Results are means ±SD. ****P<0.0001 vs WT (same collection day) by two-way ANOVA with multiple comparisons.

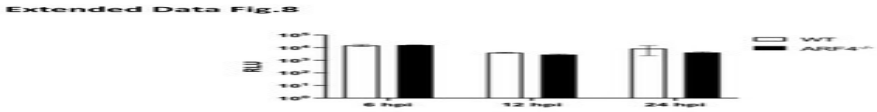

Extended Data Fig.8 ARF4 is not involved in ZIKV genomic replication. Vero WT and ARF4$^{-/-}$ cells were transfected with ZIKV replicons. Cells were lysed at indicated timepoints after transfection for luminescence measurement.

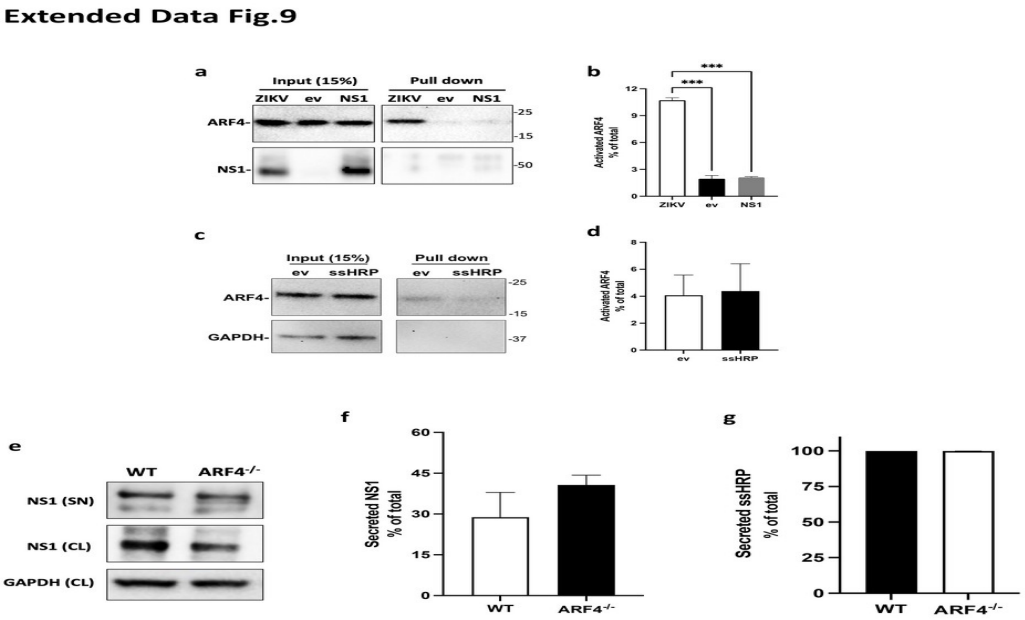

Extended Data Fig.9 ARF4 is not necessary for bulk protein secretion via the constitutive pathway. a-b) CL were collected from ZIKV NS1 transfected cells to perform GST pull down using GST fused VHS-GAT bait. CL and eluates, as input and pull-down samples respectively, were subjected to WB using ARF4 antibodies. CL from empty vector-transfected and ZIKV-

infected cells, serving as a negative and positive controls respectively, were subjected to the same assay. GAPDH was used as loading control. ARF4 activity was calculated as the percentage of activated ARF4 in eluates relative to total ARF4 in CL. **c-d)** ARF4 activation was detected as described above using ssHRP transfected Vero cells. **e-g)** NS1 and ssHRP in SN and CL were either detected by anti-NS1 antibody or quantified by using a Microbeta luminometer. Secretion of NS1 or ssHRP was calculated as the percentage of total amount (SN+CL). Data are shown as mean ± SD. ***P<0.001 by two-way ANOVA with multiple comparisons.

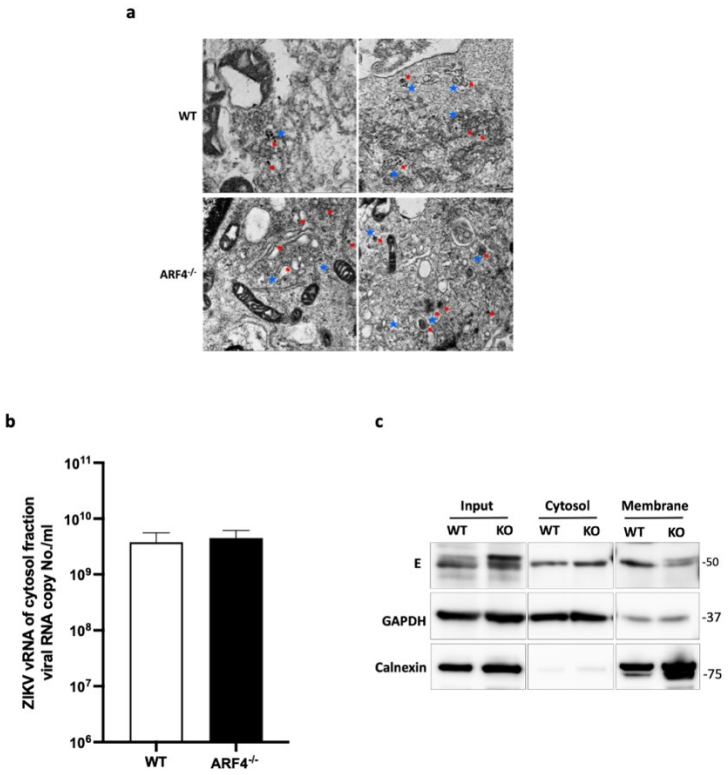

Extended Data Fig.10 ARF4 does not affect the viral assembly. a) ZIKV infected Vero WT and ARF4$^{-/-}$ cells were fixed at 24hrs after infection (MOI=10) to perform TEM. Newly formed virions are indicated by red arrows and ER invaginations containing viral particles are indicated by blue stars. Scale bar, 500nm. **b-c)** Freeze-and-thaw (F&T) was performed using ZIKV infected(b)/ RSPs-producing (c) Vero WT and ARF4$^{-/-}$ cells. Isolated cytosol factions (b) were subjected to to RT-qPCR to measure viral RNA copy no. Data are shown as mean ± SD. E protein (c) was detected in isolated cytosol and membrane fractions as an index of formed RSPs and unpacked membrane viral protein respectively. GAPDH and Calnexin were detected as cytosol and membrane markers.

Extended Data Fig.11 ARF4 deletion interrupts ZIKV prM cleavage. Vero WT and ARF4$^{-/-}$ cells were infected by ZIKV at a MOI of 10. CL were collected at indicated timepoints post infection to performed WB using antibodies against both prM and cleaved M proteins. GAPDH is used as loading control.

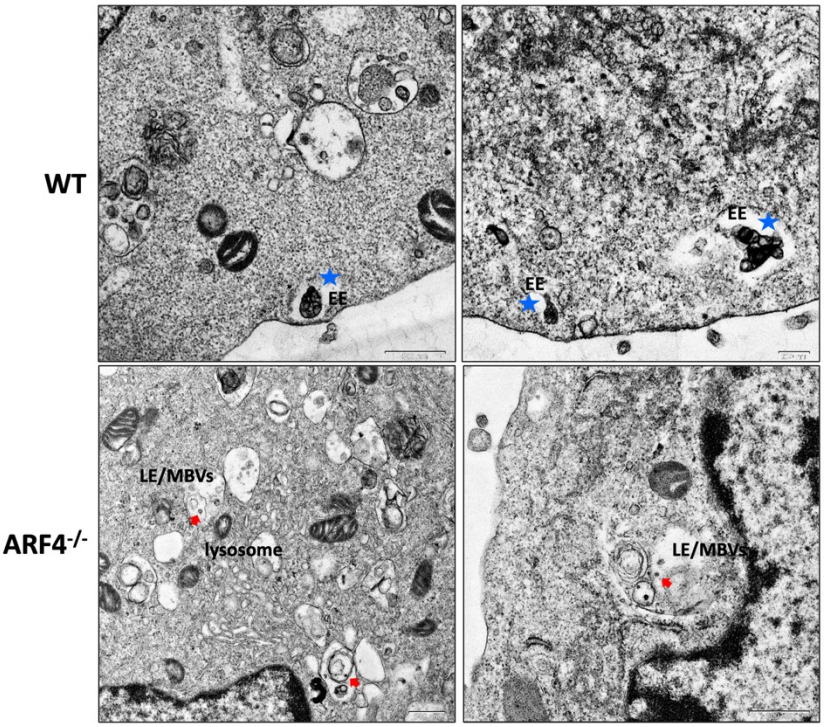

Extended Data Fig.12 ARF4 regulates sorting of newly formed viral particles during intracellular transport. ZIKV infected Vero WT and ARF4$^{-/-}$ cells were fixed at 24hrs after infection (MOI=10) to perform TEM. Accumulated virions were observed as clusters in EE like compartments in Vero WT cells (upper panel indicated by blue star). Individual or a cluster of virions were visualized in LE/MBVs compartments surrounded by lysosomes in ARF4$^{-/-}$ cells (lower right panel indicated by red arrows).

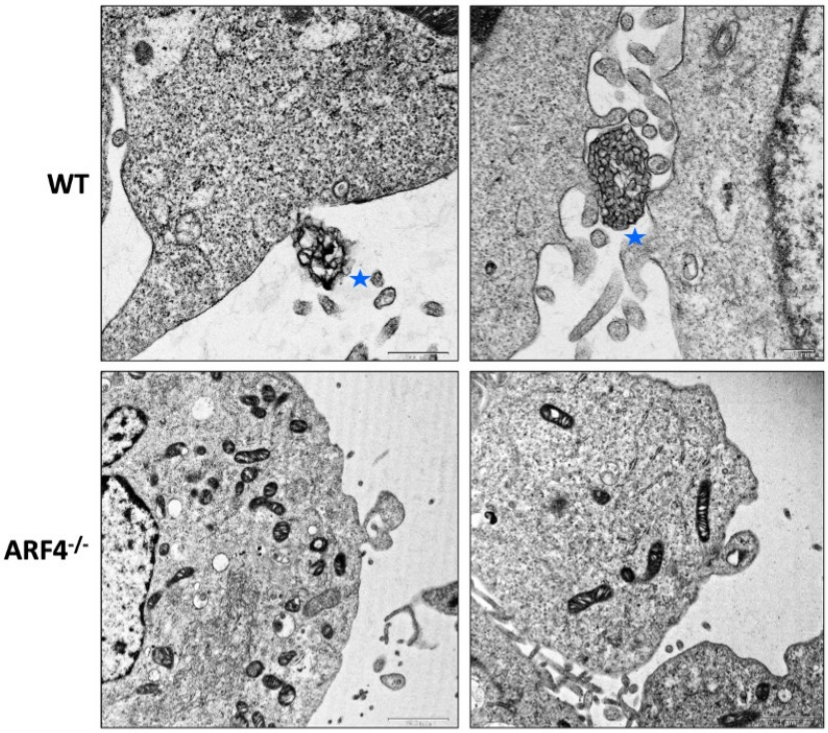

Extended Data Fig.13 Secretion of ZIKV progeny virions are observed by TEM in Vero WT, but not ARF4$^{-/-}$ cells. ZIKV infected Vero WT and ARF4$^{-/-}$ cells were fixed at 24hrs after infection (MOI=10) to perform TEM. A cluster of membrane packed virions was observed to be budding off from the cell membrane only in infected WT cells (indicated by blue stars).

Extended Data Fig.14

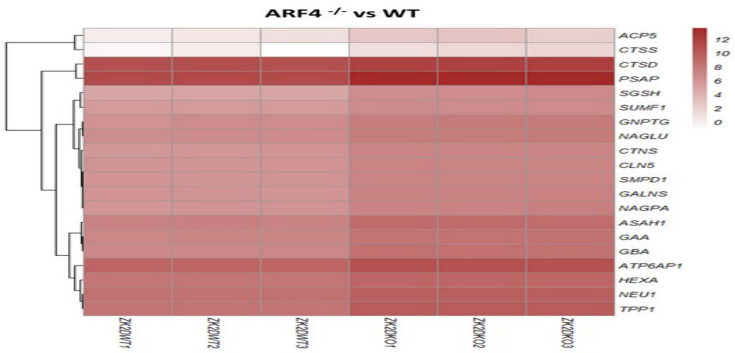

1053

1054 **Extended Data Fig.14 Heatmap analyses indicates the top 20 genes enriched in the**
1055 **lysosome pathway, upregulated in ARF4 knockout group compared to WT group** Heatmaps
1056 of gene expression levels shows as log2(gene expression).

Extended Data Fig.15

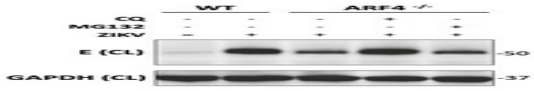

1057

1058 **Extended Data Fig.15** Cell lysates were collected at 24hrs post infection to perform WB using
1059 anti-E antibody, showing comparable levels of total E proteins between different treatment
1060 conditions. GAPDH was used as loading control.

Extended Data Fig.16

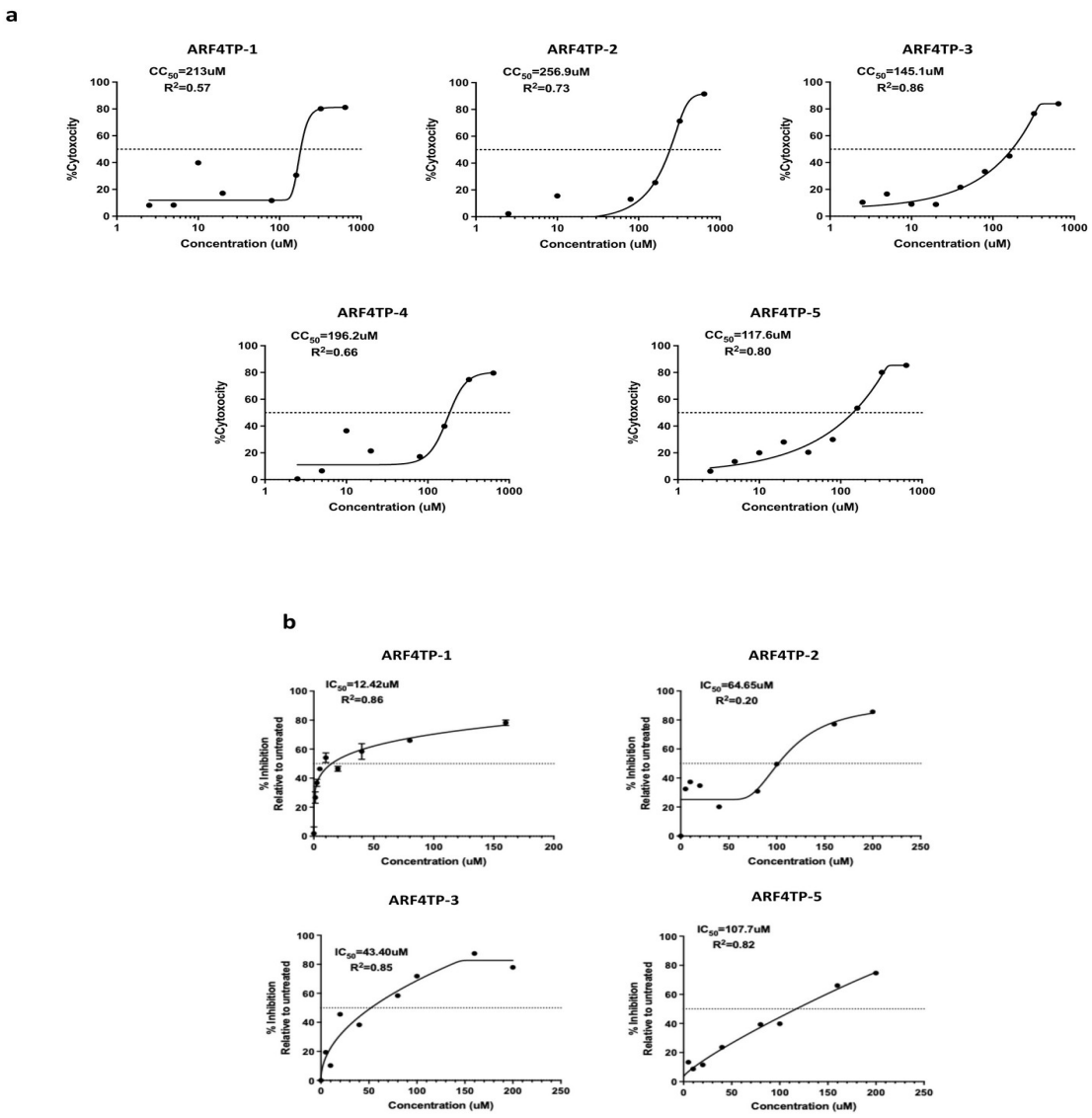

1061

1062 **Extended Data Fig.16 CC_{50} (a) and EC_{50} curves of ARF4 targeting peptides (ARF4TPs)**

1063

1064 **Extended Data Fig.17 CC50 (a) and IC50 (b) curves of ARF4TP-4 measured in human HeLa**
1065 **cells.**

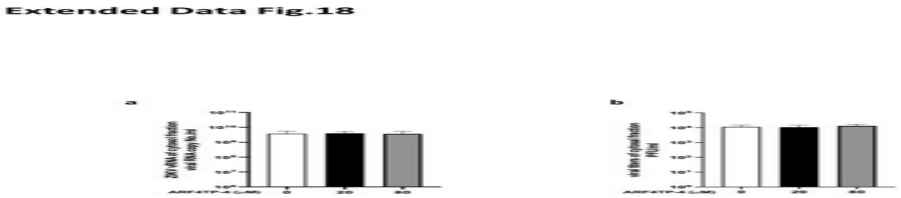

1066

1067 **Extended Data Fig.18 ARF4TP-4 does not affect viral assembly.** Freeze-and-thaw (F&T) was
1068 performed as described in the methods section using ZIKV infected Vero cells treated with
1069 ARF4TP-4 at indicated concentrations. Isolated cytosol factions were subjected to to RT-qPCR
1070 (b) and plaque assay (c) to measure the viral RNA copy No. and infectious particles. Data are
1071 shown as mean ± SD.

Extended Data Fig.19

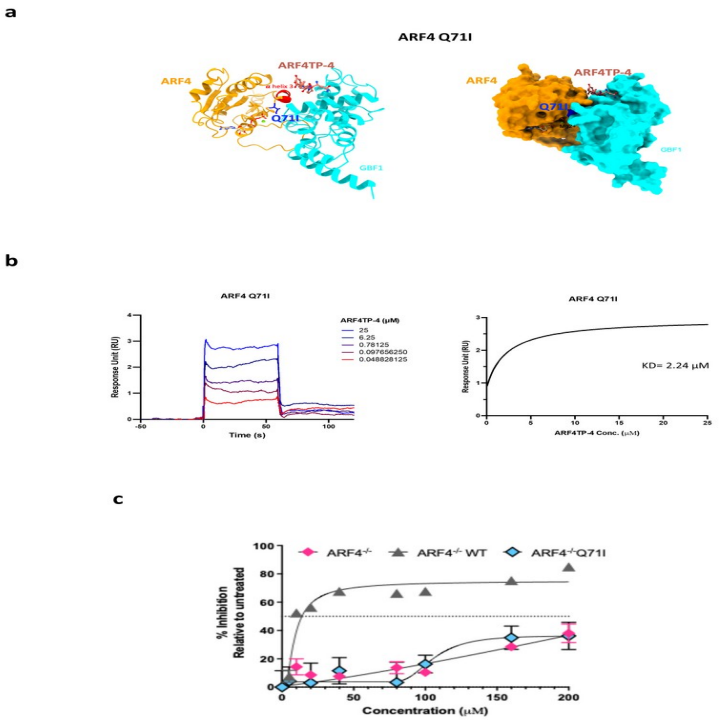

1072

1073 **Extended Data Fig.19 ZIKV secretion is not sensitive to ARF4TP-4 treatment in ARF4-Q71I**
1074 **re-expressing cells**. **a)** 3D visualization of putative interaction of ARF4TP-4 with ARF4-Q71I.
1075 ARF4 is rendered as a cartoon and coloured in orange, in which the α-helix 3 is highlighted in
1076 red. The mutated residue-Q71I is coloured in blue. GBF1 is rendered as a cartoon and
1077 coloured in cyan. The peptide QVYPL is rendered as a ball-stick and coloured in salmon. **b)**
1078 Binding of ARF4TP-4 to ARF4-Q71I was measured by Surface Plasmon Resonance (SPR).
1079 Graphs of equilibrium response units versus compound concentrations are plotted. **c)**
1080 Inhibition by ARF4TP-4 was detected following the same methods as the IC50 assay, but
1081 using ZIKV-infected Vero ARF4$^{-/-}$ and re-expressed ARF4 WT or Q71I cells respectively.

Extended Data Fig.20

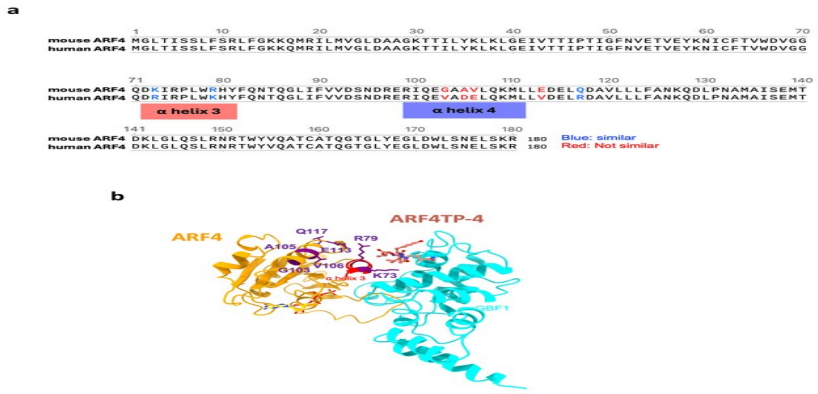

1082

1083 **Extended Data Fig.20 ARF4TP-4 is expected to function in mouse ARF4. a)** Sequence
1084 alignment of human and mice ARF4 proteins. **b)** The 3D visualization of putative interaction
1085 of ARF4TP-4 with mouse ARF4. ARF4 is rendered as a cartoon and coloured in orange, in
1086 which the α-helix 3 is highlighted in red. GBF1 was rendered as a cartoon and coloured in
1087 cyan. The peptide QVYPL is rendered as a ball-stick model and coloured in salmon. Different
1088 AAs are highlighted in purple.

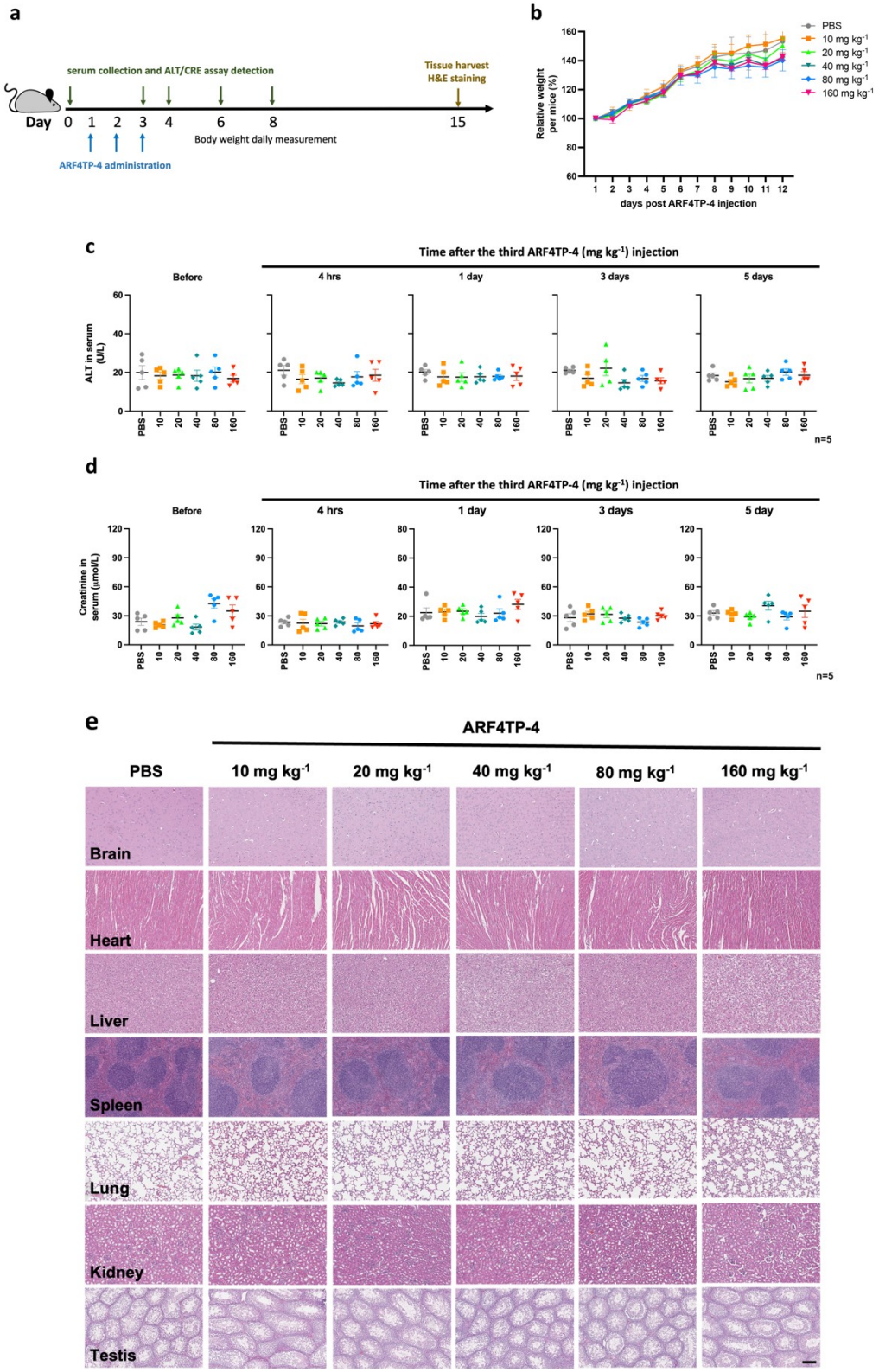

1089

1090 **Extended Data Fig.21 ARF4TP-4 is safe for mice a)** Schematic of safety experiments in mice.

1091 **b)** Body weight of PBS or ARF4TP-4 treated mice were measured daily till 12 days post last

injection. Date are means ±SD. **c-d)** The ALT (c) and creatinine (d) in the sera collected at indicated day from PBS or ARF4TP-4 injection mice were calculated by using the ALT assay kit and creatinine kit (NJJCBIO). All error bars reflect ±SD. **e)**Tissues were collected and fixed by 4%PFA for H&E staining at 12 days post the 3rd ARF4TP-4 injection.

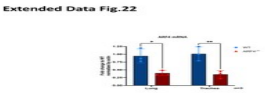

Extended Data Fig.22 ARF4 mRNA is significantly reduced in ARF4$^{-/+}$ mice. ARF4 transcription was detected by RT-qPCR using total RNA isolated from lung and testis collected from WT and ARF4$^{-/+}$ mice.

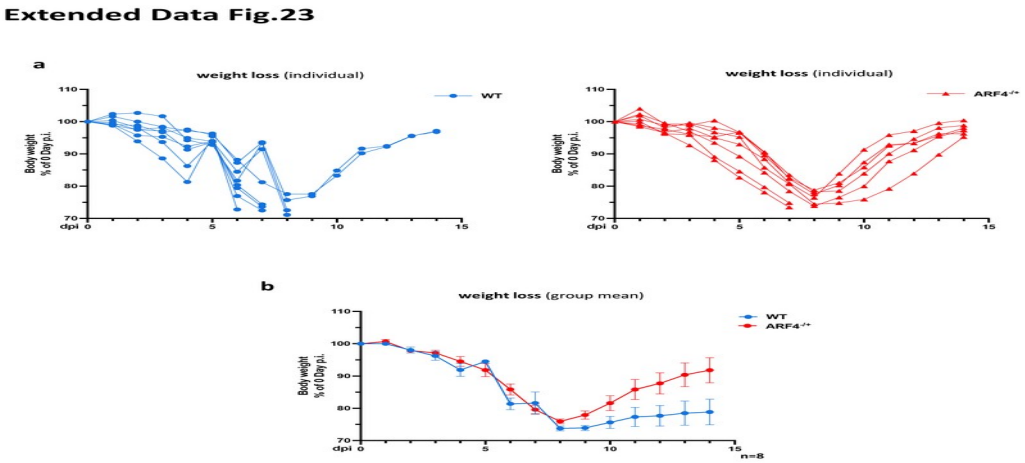

Extended Data Fig.23 Body weight loss induced by IAV recovers in ARF4-/+ mice. Body weight was measured daily after IAV challenge in both wide-type (WT) and in ARF4-/+ mice for 14 days or till the body weight reduction was up to 25%. For group mean plots in b , weight loss is shown as mean change in body weight ((± SEM).

Extended Data Fig.24

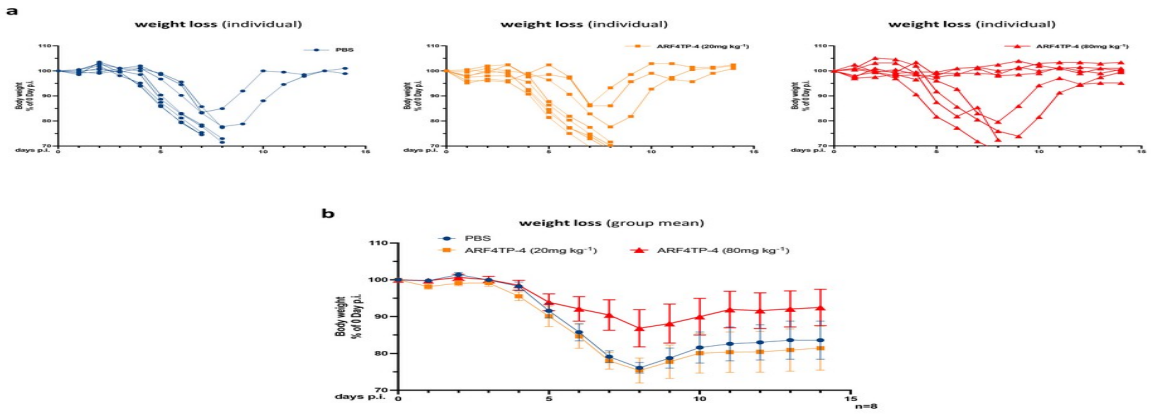

Extended Data Fig.24 ARF4TP-4 prevents body weight loss after IAV challenge. ARF4TP-4 treatment and IAV challenge were performed as described in Fig 6j. Body weight daily monitor was performed in both wide-type (WT) and in ARF4TP-4-treated mice for 14 days post IAV inoculation or till the body weight reduction was up to 25%. For group mean plots in b , weight loss is shown as mean change in body weight ((± SEM).